Received: 17 May 2020 | Revised: 14 July 2020 | Accepted: 16 July 2020

DOI: 10.1002/wcms.1500

ADVANCED REVIEW

WIREs COMPUTATIONAL MOLECULAR SCIENCE WILEY

High-throughput computational design of halide perovskites and beyond for optoelectronics

Yuheng Li[1] | Kesong Yang[1,2,3]

[1]Department of NanoEngineering and Program of Chemical Engineering, University of California San Diego, La Jolla, California

[2]Program of Materials Science and Engineering, University of California San Diego, La Jolla, California

[3]Center for Memory and Recording Research, University of California San Diego, La Jolla, California

Correspondence
Kesong Yang, Department of NanoEngineering and Program of Chemical Engineering, University of California San Diego, La Jolla, CA 92093-0448.
Email: kesong@ucsd.edu

Funding information
National Science Foundation, Grant/Award Number: ACI-1550404

Abstract

Halide perovskites have attracted great interest as promising next-generation materials in optoelectronics, ranging from solar cells to light-emitting diodes. Despite their exceptional optoelectronic properties and low cost, the prototypical organic–inorganic hybrid lead halide perovskites suffer from toxicity and low stability. Therefore, it is of high demand to search for stable and nontoxic alternatives to the hybrid lead halide perovskites. Recently, high-throughput computational materials design has emerged as a powerful approach to accelerate the discovery of new halide perovskite compositions or even novel compounds beyond perovskites. In this review, we discuss how this approach discovers halide perovskites and beyond for optoelectronics. We first overview the background of halide perovskites and methodologies in high-throughput computational design. Then, we focus on materials properties for different optoelectronic applications, and how they are assessed with materials descriptors. Finally, we review different studies in terms of specific materials types to discuss their design principles, screening results, and experimental verification.

This article is categorized under:
Structure and Mechanism > Computational Materials Science
Electronic Structure Theory > Density Functional Theory

KEYWORDS

computational materials design, high-throughput, light-emitting, machine learning, perovskite, solar cell

1 | INTRODUCTION

Lead halide perovskites have emerged as stellar next-generation materials for a wide range of optoelectronic applications, including solar cells, light-emitting diodes (LEDs), transistors, lasers, and so on.[1–6] This class of materials has a common chemical formula of $APbX_3$, in which A is an organic cation (e.g., $CH_3NH_3^+ = MA^+$, $CH[NH_2]_2^+ = FA^+$) or a large inorganic cation (e.g., Cs^+) and X is a halide anion. They adopt the perovskite structures that consist of a three-dimensional framework of corner-sharing PbX_6 octahedral. Since the debut of $MAPbI_3$ and $MAPbBr_3$ as photovoltaic materials,[1] the power conversion efficiency (PCE) of lead halide perovskite solar cells have rapidly reached 25.2%.[7] The success of this class of materials is largely attributed to their exceptional properties like proper and tunable bandgaps, large optical absorption coefficients, long diffusion lengths, small and balanced charge carrier effective masses, compositional flexibility, high defect tolerance, and low-temperature solution processability.[8–16]

Despite their great promise in optoelectronic applications, lead halide perovskites are confronted with two major problems that hinder their large-scale commercialization, namely low stability and toxicity of lead.[8,17,18] One intrinsic solution to these problems is to find stable and lead-free alternatives that possess similar optoelectronic properties with lead halide perovskites.[19–25] This solution requires comprehensive searches in large compositional and structural spaces, which would be too expensive in terms of time and cost for traditional trial-and-error experiments. Therefore, computational efforts are in demand for the design and discovery of effective lead halide perovskite alternatives.

In recent years, high-throughput (HT) computational materials design has become an effective and efficient approach to the discovery of novel functional materials, thanks to the development of computation power. It has been applied in various materials for broad application areas, including topological insulators, thermoelectric materials, transparent conducting oxides, two-dimensional electron gas, heusler magnets, halide perovskite optoelectronic, and so on.[26–38] This approach uses first-principles calculations to build large-scale databases for existing and hypothetical materials, and promising candidate materials are then selected from the databases using data-driven methods. The selection process relies on materials descriptors that are computationally viable and accurately describe desired materials properties for target applications. Therefore, careful development of materials descriptors is the key to successful HT computational design. There are many well-developed software frameworks to assist the large-scale computation and data analysis in HT computational design. A few examples are AFLOW,[39] pymatgen,[40] the Atomic Simulation Environment,[41] and MatCloud.[42] There are also online materials databases built from first-principles calculations, including AFLOWLIB,[39] Materials Project,[43] Open Quantum Materials Database (OQMD),[44] and Computational Materials Repository.[45]

The HT computational design approach has seen successful applications in the search of stable and nontoxic alternatives to lead halide perovskites for optoelectronic applications. Various HT studies have explored enormous compositional and structural spaces using different materials descriptors, calculation methodologies, and screening processes. It has become necessary to summarize these different studies and discuss the effective design principles to provide informative guidance for computational and experimental design of new materials. In addition, a large number of promising candidates designed from the HT studies need to be categorized for the convenience of researchers in the broad field of halide perovskite optoelectronics to conduct further theoretical and experimental research as well as practical applications. Therefore, in this review article, we first overview common materials descriptors and their computational viability for halide perovskites and beyond for optoelectronics, which are vital for the HT computational design. Then, specific HT studies are reviewed with an emphasis on their design principles, screening processes, and results. The studies are classified in terms of IVA element-based single perovskites, other element-based single perovskites, double perovskites, and perovskite derivatives. We also review HT computational studies incorporating machine learning (ML) as a separate subsection. The selected candidates from all the HT studies reviewed are summarized in Tables 1–4. Finally, we provide our own view and outlook in this flourishing field.

2 | MATERIALS PROPERTIES AND MATERIALS DESCRIPTORS

Materials properties direct the design of specific classes of materials for specific applications. In the design of halide perovskite-like materials for optoelectronics, properties of stability and nontoxicity are considered for solving the common challenges faced by prototypical lead halide perovskites, and optical and electronic properties determine essential functionalities of materials in the optoelectronic applications. In HT computational design, materials properties are described using computationally viable descriptors. The descriptors filter a large calculated materials repository and select candidates with desired properties, playing critical roles in applying HT computational design in specific materials applications. In this section, we briefly review the desired materials properties for halide perovskites and beyond for optoelectronics, and how these properties are accessed through calculated descriptors in HT computational design.

2.1 | Stability

Evaluating structural stability (or formability) of the perovskite structures for different chemical compositions has been one main screening process in many studies.[50,60,61] There are empirical descriptors of octahedral factor $\mu = r_B/r_X$ and Goldshmidt tolerance factor $t = (r_A + r_X)/\sqrt{2}(r_B + r_X)$ that use ionic radii to predict the perovskite formability.[62]

Recently, researchers have defined effective ionic radii for organic cations,[63,64] and revised the Shannon radii for cations in halide systems.[65,66] In 2019, Bartel et al. proposed a new machine-learned tolerance factor $\tau = \frac{r_X}{r_B} - n_A\left(n_A - \frac{r_A/r_B}{ln(r_A/r_B)}\right)$ that show higher prediction accuracy than the traditional t.[67] Notably, τ uses Shannon radii and change monotonically with perovskite formability.

High thermodynamic stability is essential for computationally predicted materials. It is especially important when designing alternative materials to the intrinsically unstable lead halide perovskites.[68] In HT design, the descriptors of formation enthalpy (ΔH_f) and decomposition enthalpy (ΔH_d) are usually used.[69,70] ΔH_f describes energy change from elemental component to compound, and positive values indicate unstable compounds. ΔH_d describes whether the compound tends to decompose into various elemental, binary, ternary, or more complex components, and negative values indicate unstable compounds. A rigorous determination of ΔH_d must consider all existing compounds in the Inorganic Crystal Structure Database (ICSD) and even hypothetical compounds as potential decomposition products and scrutinize all possible decomposition pathways to avoid overestimation of the thermodynamic stability.[71–73] A comprehensive way to predict thermodynamic stability based on ΔH_d is to construct phase diagrams using the convex hull method.[74,75]

Dynamic stability represents a more realistic evaluation of material stability in the working environment. Computationally, phonon calculations[76] and ab initio molecular dynamics (AIMD)[77] are two main methods to assess materials' dynamic stability. In detail, the finite-temperature phonon spectrum can be calculated using density functional perturbation theory (DFPT), and imaginary frequencies in the phonon spectrum indicate dynamical instability. AIMD calculations show total energy evolutions at finite temperature as a function of time, and also give crystal geometry change with time, from which the dynamic stability can be observed. These calculations are expensive in terms of time and cost and are usually performed only for preselected candidates in HT screening processes.

2.2 | Optoelectronic properties

The bandgap is one of the most important electronic properties for optoelectronic materials because it directly determines how the materials interact with light (e.g., absorb or emit light). Bandgap energy determines the energy of the photons being emitted or absorbed, and the bandgap type determines whether phonons are required in the interactions with light. Different optoelectronic applications require different bandgap characteristics. The two most prevalent applications of halide perovskites serve as good examples. For photovoltaics, the optimal bandgap energy for single-junction solar cells is 1.34 eV according to the Shockley–Queisser (S-Q) detailed-balance model.[82,83] Type of bandgap can be either direct or indirect for photovoltaics.[69] For light-emitting, bandgap energy determines the photon energy for the desired color of light by the equation $E_{photon} = E_g + k_BT/2$, and direct bandgap type is required for high emission efficiency.[6] The calculation of bandgap energy has different levels of theory. The standard density functional theory (DFT) calculations using the Perdew–Burke–Ernzerhof (PBE)[84] functional within the generalized gradient approximation (GGA) is computationally efficient but severely underestimate bandgap energy, while hybrid functional within Heyd–Scuseria–Ernzerhof (HSE) formalism give more accurate results but are more time-consuming.[85] Spin–orbit coupling (SOC) is also very important in halide perovskite systems containing heavy elements.[86] Most HT studies screen materials on bandgaps calculated at GGA-PBE level and perform HSE and SOC calculations for a relatively small amount of candidates.

Electron and hole effective masses are directly related to their mobility. They are required to be small and balanced for efficient transport of photogenerated carriers in solar cell materials. In methylammonium lead iodide perovskite ($MAPbI_3$), effective masses of both electrons and holes are very small, granting the material long-range ambipolar transport property.[87] One method to determine effective masses is to fit calculated band structures near band edges using the equations $\frac{1}{m^*} = \frac{1}{\hbar^2}\frac{\partial^2 E}{\partial k^2}$. Visually, a more dispersive band indicates smaller effective mass. Another method is to calculate through the semiclassical Boltzmann transport theory.[50] Interestingly, Xiao et al. brought up the concept of electronic dimensionality, which can be used to understand isotropic/anisotropic current flow and different effective masses in materials.[88]

Exciton binding energy is the energy needed to separate electron–hole pairs. A small exciton binding energy is beneficial for exciton separation into free carriers in photovoltaics, and a large one is beneficial for charge recombination to emit light. Exciton binding energy in HT computational studies is usually approximated using the hydrogen-like Wannier–Mott model, which sees it as an effective Rydberg: $E_B = \frac{\mu^* R_y}{m_0 \varepsilon_r^2}$.[50,89] In the equation, ε_r is the relative dielectric

constant. It is usually adopted by the high-frequency limit of the dielectric constant (ε_∞) contributed by electronic polarization and calculated using finite-electric field and Berry-phase calculations.[69]

Halide perovskites have extremely high optical absorption coefficients, which greatly contribute to their high efficiency as solar cell absorbers.[62,90,91] The optical absorption coefficients can be calculated using the equation[92]:

$$\alpha(\omega) = \sqrt{2}\frac{\omega}{c}\sqrt{\sqrt{\varepsilon_1(\omega)^2 + \varepsilon_2(\omega)^2} - \varepsilon_1(\omega)}, \quad (1)$$

where c is the speed of light, ω is the photon frequency, and $\varepsilon_1(\omega)$ and $\varepsilon_2(\omega)$ are the real part and imaginary part of the complex dielectric function. $\varepsilon_1(\omega)$ and $\varepsilon_2(\omega)$ can be calculated from ground-state electronic structure calculations.[93,94] More accurate description of optical properties requires GW approximation and the Bethe–Salpeter equation (BSE),[95,96] which are very time-consuming and usually beyond the scope of HT computational design.

2.3 | Defect properties

Point defects could create nonradiative electron–hole recombination centers and deteriorate quantum efficiencies in solar cells and light emitters.[14] Intrinsic point defects can be categorized into vacancies, interstitials, and antisites. Taking a typical A-M-X ternary system as an example, there could be three types of vacancies (V_A, V_M, and V_X), three types of interstitials (A_i, M_i, and X_i), and six types of antisites (A_M, M_A, A_X, X_A, M_X, and X_M). These defects should be considered on all possible nonequivalent lattice sites when building models for calculations. In calculations, defect tolerance level of optoelectronic materials can be evaluated by calculating defect formation energy (E^f) and transition energy level ($\varepsilon(q1/q2)$) (Equations (2) and (3), respectively).[97]

$$E^f[X^q] = E_{tot}[X^q] - E_{tot}[\text{bulk}] - \sum_i n_i\mu_i + qE_F + E_{corr} \quad (2)$$

$$\varepsilon(q1/q2) = \frac{E^f(X^{q1}; E_F = 0) - E^f(X^{q2}; E_F = 0)}{q2 - q1} \quad (3)$$

In the equations, X denotes a defect, q denotes a charge state, E_{tot} is total energy, μ is chemical potential, and E_F is Fermi energy. E_{corr} is a correction term based on different theories and methods, including image charge correction, potential alignment correction, band filling correction, and so on.[97–101] In a material, if defects with low formation energies do not create deep transition levels and defects that create deep levels have high formation energies, the material is defect tolerant and suitable for optoelectronic applications.[94] HT calculations of charged point defects are possible with reasonably sized supercells.[50,94,102] There are also tools like PyCDT built for integrated point defect calculations.[100] Notably, linear and planar defects are usually out of the scope of HT computational studies.

3 | HT MATERIALS DESIGN

As discussed above, the key materials properties for optoelectronics are computationally accessible through descriptors. Therefore, it is viable to perform HT computational design of halide perovskites and beyond for optoelectronics. In this section, we review HT research examples classified by materials composition and structure of interest.

3.1 | IVA element single perovskites

In 2015, Krishnamoorthy et al. screened inorganic halide perovskites for light harvesting.[46] As the first step, the authors built a total number of 360 AMX_3 compounds, with A occupied by K, Rb, and Cs, X occupied by Cl, Br, and I, and M occupied by 40 divalent cations. Then, first-principles DFT calculations were used to determine bandgaps for the

360 compounds at PBE level. To determine selection criteria for the calculated PBE bandgaps, the authors synthesized $CsSnI_3$ and used its experimental bandgap as a calibration point, which yield a criterion of 0.2–0.7 eV. Then, nine compounds were selected according to this bandgap criteria. Next, the authors evaluated the thermodynamic stability of the nine compounds by calculating the decomposition enthalpy to simple binary phases. Finally, they found three candidates ($RbSnBr_3$, $CsSnBr_3$, and $CsGeI_3$) in addition to the synthesized $CsSnI_3$.

In 2017, Yang et al. reported a high-throughput theoretical materials selection of IVA element-based halide perovskites for photovoltaics (Figure 1).[50] First, they built about 100 compound structures from the constitution space of $AM^{IV}X_3^{VII}$, where A site is for Cs or organic cations, M^{IV} site is for three IVA elements Pb/Sn/Ge, and X^{VII} site is for three halogen ions Cl/Br/I. Next, they assessed thermodynamic stability for these compounds by calculating decomposition enthalpy for main decomposition channels. The crystallographic stability was also assessed by the Goldschmidt tolerance factor t and the octahedral factor μ. Then, they screened the candidates for direct bandgap, proper bandgap energy, low effective masses, and low exciton binding energy. Finally, the authors studied defect tolerance properties of the candidates, and five Ge-based and nine Sn-based materials were selected as final candidates.

In 2017, Kim et al. built a dataset of 1,346 organic–inorganic hybrid halide perovskites.[109] The perovskites consist of 16 organic cations, three group-IV cations, and four halide anions. The authors prepared the optimized structures, the bandgap, the dielectric constant, and the relative energies, and validated them by comparing them with existing experimental and/or theoretical data. The main objective of this study is to create an IVA element-based database of halide perovskites for future data-mining efforts to explore possible structure–property relationships.

3.2 | Other element-based single perovskites

In 2016, Filip et al. explored the replacement of lead in halide perovskites by all homovalent metal ions over the entire periodic table (Figure 2).[78] The authors performed a systematic screening based mainly on the stability and the bandgap. As the first step, the authors selected B-site metals that could form BX_2 salt, which yielded 248 metal-halide combinations. Next, they excluded rare-earth and radioactive B-site metals, which downsized the combinations set to 116 compounds. Next, compounds with DFT/LDA calculated bandgaps larger than 3.5 eV were discarded, and the number of candidates left was 40. Then, the authors assessed the dynamic stability by displacing and relaxing the structures and selected 32 compounds. Then, they calculated bandgap with SOC and lowered the criteria to 2 eV, and also examined the band structures. The tolerance factor t and the octahedral factor μ were also analyzed. Finally, the authors selected 25 candidates out of the 248 compounds, and 15 of the candidates had not been proposed for

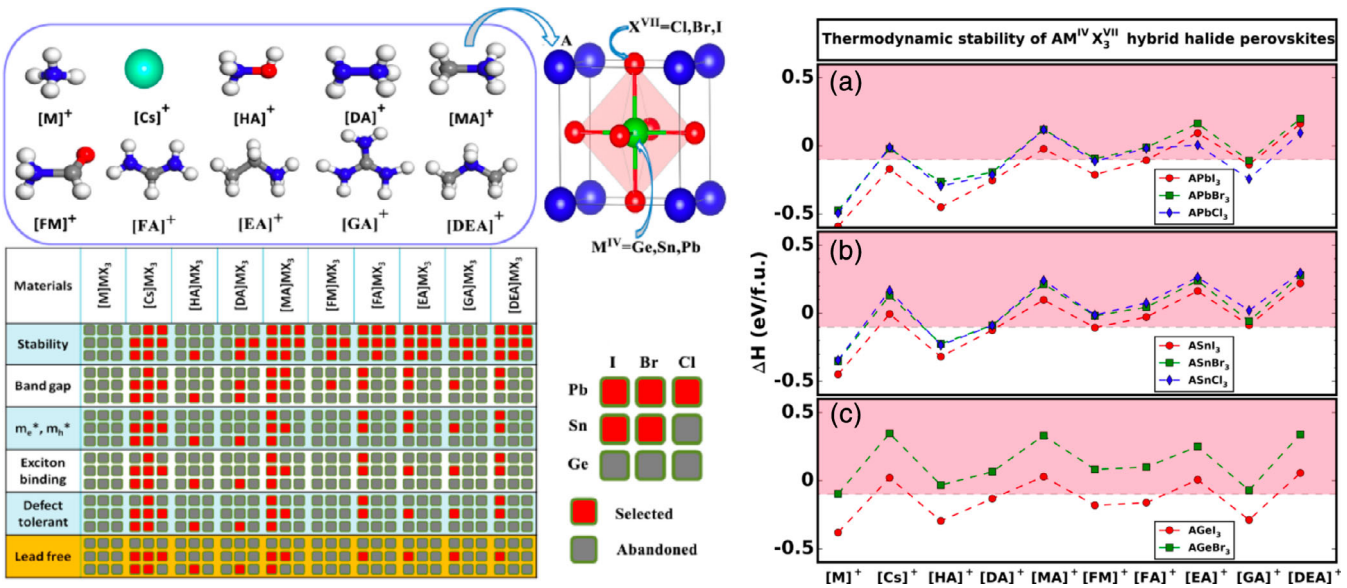

FIGURE 1 (Left) Constitution space, step-by-step screening process, and (right) calculated decomposition enthalpies. (Reprinted with permission from Reference 50 Copyright 2017 American Chemical Society)

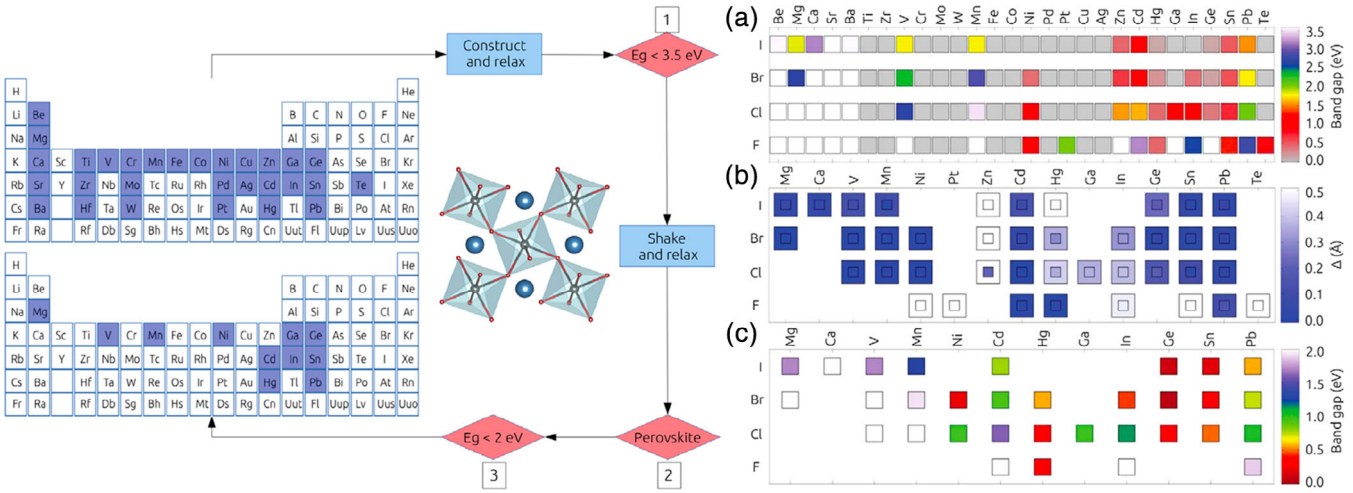

FIGURE 2 (Left) Schematic representation of the computational screening process, (right) scalar relativistic bandgaps calculated for each structure, plot of the difference between the maximum and minimum metal-halide bond length, bandgaps calculated for the remaining structures. (Reprinted with permission from Reference 78 Copyright 2016 American Chemical Society)

optoelectronics. Specifically, the authors identified Mg partial replacement as a potential pathway to less toxic halide perovskites with bandgap tunable by A-site cation.

In 2018, Ali et al. presented a systematic DFT study on the replacement of Pb in the perovskite $MAPbI_3$.[80] Besides replacements with IVA elements, they also explored replacements with almost all elements from groups I to VIII, and even binary-element replacements in different ratios. In this work, the authors used tetragonal $2 \times 2 \times 2$ $MAPbI_3$ supercell as an initial structure for Pb substitution. For single-element, the lanthanide-actinide series and some toxic elements were excluded. For binary-element, the authors focused on mixing of Ca(Zn) and Si in ratios of 1:7, 3:5, and 4:4. To search for promising photovoltaic candidates, the authors first evaluated the structural and chemical stabilities using tolerance factor and decomposition enthalpy, respectively. Then, the authors calculated the optical absorption efficiency and band structure. Finally, they concluded that for single-element replacements, IVA-group elements are better than the other elements for solar cells. For binary-element replacements, they highlighted three candidates $MACa_{0.5}Si_{0.5}I_3$, $MACa_{0.125}Si_{0.875}I_3$, and $MAZn_{0.5}Si_{0.5}I_3$ for tandem bottom cell, the best alternatives to $MAPbI_3$, and tandem top cell, respectively. The authors also noted that the ratio adjustment of Ca/Si and Zn/Si indicates a way to tune the photovoltaic performance.

In 2019, Jacobs et al. calculated 1845 halide perovskites and searched for stable and nontoxic candidates for solar cell absorbers.[59] In this work, the screening process includes five descriptors: nontoxicity, thermodynamic stability analyzed using convex hull under realistic PV operating environment, calculated bandgap at PBE level, and estimated HSE bandgap, explicitly calculated bandgap energy at HSE level, predicted PV efficiencies (above 22.7%). After screening, there were 15 materials (including three metastable materials) satisfying all criteria for single-junction solar cells, among which 13 materials have not been studied before. Due to the diverse composition space considered, especially various alloying at the perovskite A, B, and X sites, most of the 13 new candidates have mixed A- or B-site cations. Interestingly, the authors also searched for materials for silicon-perovskite tandem cells and quantum dot cells, and found 13 and 26 candidates, respectively.

3.3 | Double perovskites

In 2017, Zhao et al. exploited a cation-transmutation strategy to replace two Pb atoms with a pair of one M^+ and one M^{3+} atoms in halide perovskites, which forms double perovskites $A_2M^+M^{3+}X_6^{VII}$ (Figure 3).[70] The authors performed first-principles calculations for this class of materials with B^{3+} are Sb^{3+} and Bi^{3+}, and B^+ are eight IA, IB, and IIIA elements. They first probed the energetics of spatial distribution of $M^+X_6^{VII}$ and $M^{3+}X_6^{VII}$ octahedral. Then, the tolerance factor t and octahedral factor μ were considered for crystallographic stability. Thermodynamic stability was evaluated by calculating decomposition enthalpy with respect to different decomposing pathways of the double perovskites into

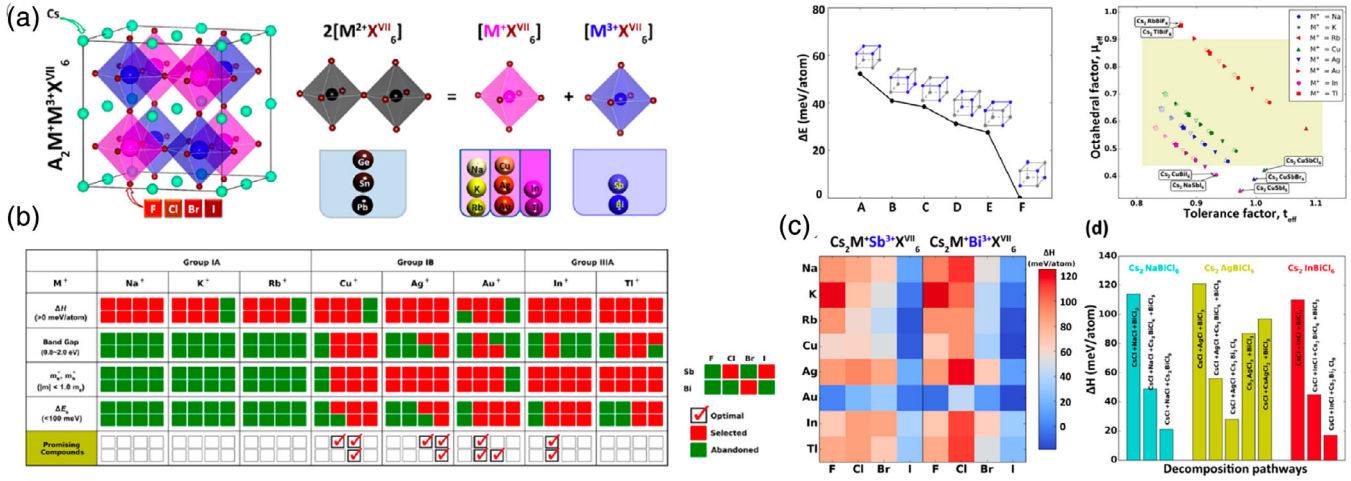

FIGURE 3 (Left) Space of candidate perovskites for materials screening and materials screening process by considering gradually the properties relevant to photovoltaic performance, (right) energies of different motifs arrangements, distribution mapping of double perovskites with effective tolerance factor and octahedral factor as variables, decomposition enthalpy, and decomposition enthalpy corresponding to different decomposition pathways. (Reprinted with permission from Reference 70. Copyright 2017 American Chemical Society)

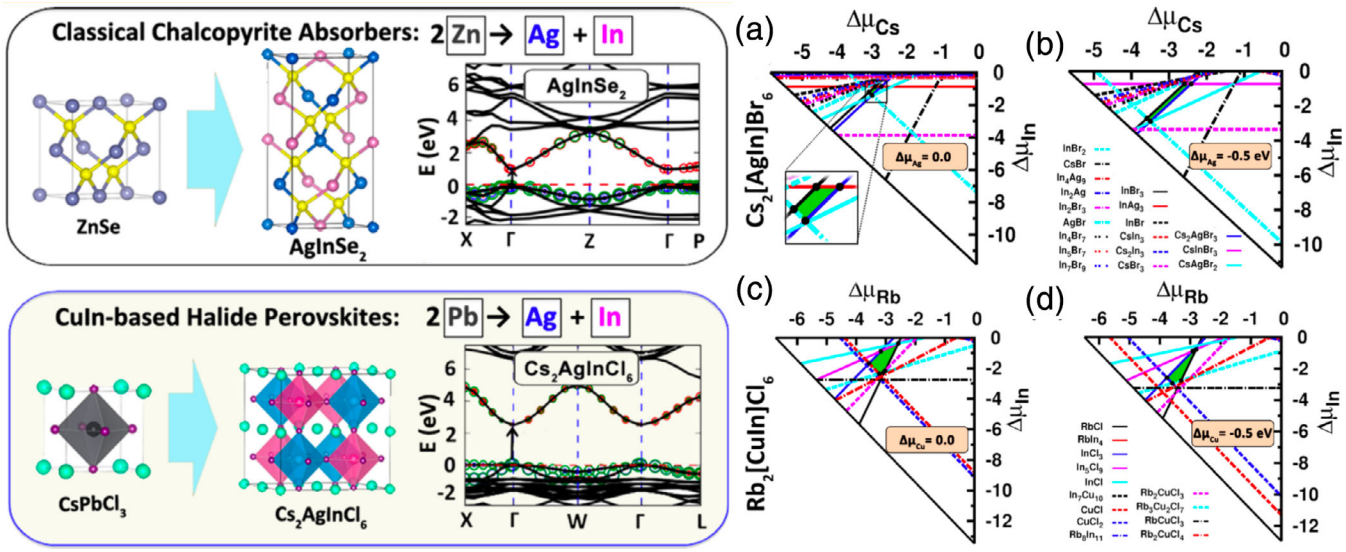

FIGURE 4 (Left) Design principles and (right) phase stability diagram analysis results sliced at several Ag/Cu-varied growth conditions. (Reprinted with permission from Reference 107. Copyright 2017 American Chemical Society)

binary and ternary compounds. Then, the authors categorized the double perovskites into three types in terms of the M^+ element group to discuss chemical trends of their electronic properties. The screening process applied photovoltaic-functionality-directed descriptors and criteria. In detail, the criteria are high thermodynamic stability, suitable bandgap in the range of 0.8–2.0 eV, charge carrier effective masses smaller than 1.0 m_0, exciton binding energy smaller than 100 meV, and nontoxicity. After screening, the authors identified 11 optimal double perovskite candidates ($Cs_2CuSbCl_6$, $Cs_2CuSbBr_6$, $Cs_2CuBiBr_6$, $Cs_2AgSbBr_6$, Cs_2AgSbI_6, Cs_2AgBiI_6, $Cs_2AuSbCl_6$, $Cs_2AuBiCl_6$, $Cs_2AuBiBr_6$, $Cs_2InSbCl_6$, and $Cs_2InBiCl_6$).

In 2017, Zhao et al. designed Pb-free halide double perovskites consisting of IB-IIIA element combinations, defined as Cu-In halide perovskite (CIHP; Figure 4).[107] The idea of transmuting two Pb to IB-IIIA elements came from the classical CuIn-Based chalcopyrite solar absorbers. Based on this idea, the authors first built a total number of 36 $A_2[BC]X_6$ CIHP compounds with B^{IB} = Cu, Ag and C^{IIIA} = Ga, In, and the A site is occupied by inorganic cations, X by halogen anions. First-principles calculations show that the CIHP double perovskites have direct bandgaps (unlike indirect gaps

in Ag-Bi double perovskites), strong valence-to-conduction band optical transition, and tunable gaps in a wide range. Then, the authors screened the 36 CIHP compounds using a series of criteria: stability against decomposition, solar bandgap values, thermodynamic stability via phase stability diagram analysis, dynamic phonon stability, and proper photovoltaic-related properties. At last, the authors identified six final candidates, three ($Cs_2AgInBr_6$, $Rb_2AgInBr_6$, and $Rb_2CuInCl_6$) of which have bandgaps close to the optimal value of 1.34 eV and simulated photovoltaic performance comparable to that of $MAPbI_3$.

In 2017, Nakajima et al. reported a high-throughput computational screening to discover low-toxic halide perovskites.[58] First, the authors performed DFT calculations for a large total number of 11,025 ABX_3 and $A_2BB'X_6$ compositions, where A is an organic or inorganic cation, B and B′ are metal elements, and X is a halogen element. The HT calculations built up a large database for screening. Then, for screening in the database, the authors excluded metallic compounds, selected perovskite structures after relaxation, limited the bandgap to the range of 0.8–2.2 eV from SOC + HSE calculations, excluded compounds with large effective masses, evaluated the band edges, and removed toxic compounds. Finally, the screening yielded 51 low-toxic halide perovskites, most of which are double perovskites. This study represents a large-scale screening based on expensive DFT calculations.

In 2018, Filip et al. calculated quaternary phase diagrams for all 18 lead-free pnictogen/noble metal halide double perovskites and explored chemical mixing to stabilize the double perovskites and lower their bandgaps.[74] The authors noted that there had been four types of double halide perovskites in terms of the B and B′ site element combinations: pnictogen and alkali metals, pnictogen and post-transition metals, post-transition and noble metals, and pnictogen and noble metals. The pnictogen/noble metal combination was of interest in this work because they have bandgaps spanning the visible spectrum and low effective masses, and some of them had been synthesized and show high stability. First, the authors systematically investigated materials stability of the perovskites by calculating the compositional phase diagrams and found that $Cs_2BiAgCl_6$, $Cs_2BiAgBr_6$, and $Cs_2SbAgCl_6$ are stable against decomposition. Then, they analyzed pseudo-ternary phase diagrams, which are slices through the quaternary phase diagram and found that mixing I, Br, or Cu in the three stable perovskites could suppress the formation of their competing ternary compounds. Finally, $Cs_2BiAg_{1-x}Cu_xCl_6$ was identified as promising stable mixed double perovskites with lowered bandgaps.

In 2019, Cai et al. built a database of inorganic halide double perovskites through HT computation and reported its application on searching for lead-free halide photovoltaic absorbers.[60] Starting from 1980 double perovskite compounds, $A_2MM'X_6$ (A = Li, Na, K, Rb, Cs, M = Li, Na, K, Rb, Cs, Cu, Ag, Au, Hg, In, Tl, M′ = Sc, Y, Al, Ga, In, Tl, As, Sb, Bi, and X = F, Cl, Br, I.), the authors evaluated their octahedral and tolerance factors as the first screening criteria. Then, 1,149 compounds were calculated using density functional theory methods for their structural, electronic, and transport properties. A database of the calculation results is incorporated in Materials Project online. To showcase an application of the database for photovoltaics, the authors further screened the compounds using criteria of low energy above the hull, appropriate PBE bandgaps, and small effective masses. After this, 30 compounds in five M-M′ categories were left for further structural and bandgap calculations using HSE and SOC. Next, optical absorption, spectroscopic limited maximum efficiency (SLME), and dynamic stability using phonon calculations were performed. Finally, the authors identified 11 solar absorber candidates from three different M-M′ categories. The candidates include $Cs_2AgInBr_6$, $Cs_2InAsBr_6$, $Cs_2InBiCl_6$, $Cs_2InBiBr_6$, $Cs_2InSbBr_6$, $Cs_2TlAsBr_6$, Cs_2TlAsI_6, $Cs_2TlSbBr_6$, Cs_2InGaI_6, $Cs_2InInBr_6$, and $Cs_2TlTlBr_6$, which are stable and have SLMEs larger than 10%. For the candidates, the authors also analyzed chemical trends of bandgaps to provide guidance on tuning electronic structure using substitutional alloying.

In 2020, Bartel et al. performed a detailed computational study of all-inorganic cesium chloride double perovskites $Cs_2BB'Cl_6$ (Figure 5).[61] To start with 903 compounds consisting of 43 possible B-site cations, the authors used the new machine-learned tolerance[67] factor to select 311 compounds that are likely to form a stable perovskite structure, among which 290 had not been synthesized. Then, the authors analyzed decomposition enthalpy using quaternary convex hull phase diagrams and found 152 stable compounds and 109 metastable compounds. It was noted that most (82%) stability-defining decomposition reactions for the double perovskites involve ternary compounds, indicating that stability analysis using only elemental and binary precursor compounds is not reliable. Next, the authors also carefully examined structural distortions in the 311 compounds to avoid inaccurate predictions of stability and electronic structure. Next, 47 (meta)stable non-toxic compounds were identified with suitable bandgaps for optoelectronic applications. Among the 47 materials, 26 were referred to as a new class of triple-alkali perovskites (TAPs, $Cs_2[alkali]^+[transition\ metal]^{3+}Cl_6$) because alkali cations occupy their B sites. The authors then characterized the electronic structure of four TAPs, $Cs_2(K,Na)(Mn,Ni)Cl_6$, using many-body GW_0 and BSE calculations, and found that they all have large exciton binding energies. The excitons are also optically accessible under a wide range of compositions, granting TAPs highly

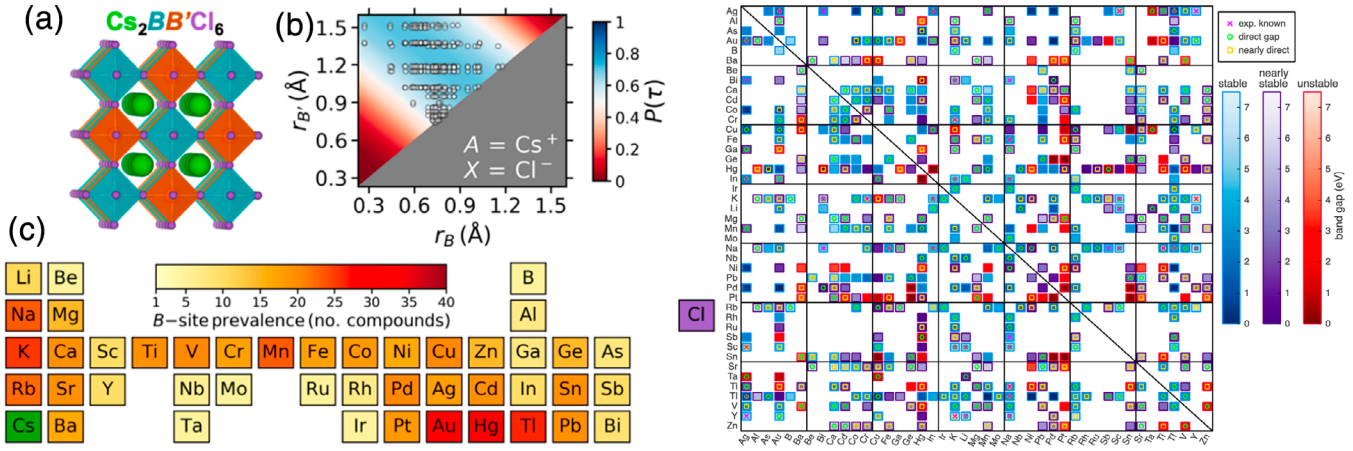

FIGURE 5 (Left) Structure of ideal rock-salt double perovskite where, range of ionic radii for the B site and B′ site, heat map of the occurrence of the 43 elements considered, and (right) map of $Cs_2BB'Cl_6$ properties. (Reprinted with permission from Reference 61. Copyright 2017 American Chemical Society)

tunable optical properties. These findings provide potential new all-inorganic halide double perovskites whose optoelectronic properties can be modulated by sublattice mixing.

In 2020, Zhang et al. calculated 980 halide double perovskites $A_2B^+B^{3+}X_6$ and explored the chemical trends in their thermodynamic stability and bandgaps.[110] First, to accurately predict the stability with respect to decomposition, the authors considered all metal halides in Materials Project[43] as competing compounds and calculated the energy above the convex hull for the 980 perovskites. The stability was analyzed with quaternary and pseudo-ternary phase diagrams, and only 112 out of the 980 double perovskites were found stable. Their results also show that 27 double perovskites predicted previously are unstable. Then, the authors showed the chemical trends in the calculated energy above hull using color maps. They found that the stability is mainly determined by A, X, and B^+ elements, that is, it increases as A becomes heavier and X becomes lighter. Next, the bandgaps were calculated by the GGA functional. The authors found that the bandgaps decrease monotonically as X becomes heavier and also change nonmonotonically with B^+ and B^{3+}. Finally, by combining the trends of stability and bandgaps, the authors provided guidance on the design of double perovskites with high stability and tunable bandgaps in a wide range.

3.4 | Perovskite derivatives

In 2017, Jain et al. screened perovskite-like lead-free compounds for optoelectronics using first-principles high-throughput computation.[111] The perovskite-like compounds have formulas of ABX_4 and $A_3B_2X_9$ besides double perovskite $A_2BB'X_6$, which were selected from solution processable materials in literature. In the formulas, monovalent A and B′ cations include Na, K, Rb, Cs Cu, and Ag, trivalent B cations include Ga, In, and Sb, and halogen X anions include Cl, Br, and I. In total, there were 480 compounds for screening. The first screening step applies calculated formation energy relative to a given compound's possible precursors, which effectively exclude unstable compounds. Second, the authors eliminated compounds with calculated GGA bandgaps larger than 2.5 eV. Then, HSE calculations were performed to further select compounds with direct bandgaps between 1.5 and 2.5 eV. Finally, 10 candidates were identified and seven of them were new. $Cs_3Ga_2I_9$ was addressed for the smallest bandgap within the visible spectrum of 1.72 eV. For the 10 selected candidates for lead-free optoelectronics, the authors presented their effective masses, density of states, and absorption coefficients.

In 2017, Tang et al. presented a design strategy of $Cs_{3+n}M(II)_nSb_2X_{9+3n}$ compounds by inserting $[MX_6]$ octahedral layers into $[Sb_2X_9]$ bilayers in $Cs_3Sb_2X_9$.[113] The authors found that Sn and Ge are promising M(II) candidates for improved photovoltaic-relevant properties of the compounds. They also found that thickness adjustment of the inserted layers can tune the compounds' bandgaps and effective masses. Later in 2019, Liu et al. studied $A_4MM'_2X_{12}$ compounds by computational screening of different element combinations, namely A = (K^+ and Cs^+), M = (Zn^{2+} and Sn^{2+}), M′ = (Bi^{3+} and Sb^{3+}), and X = (Cl^-, Br^-, and I^-).[114] The authors first determined the ground-state scaffold structure of

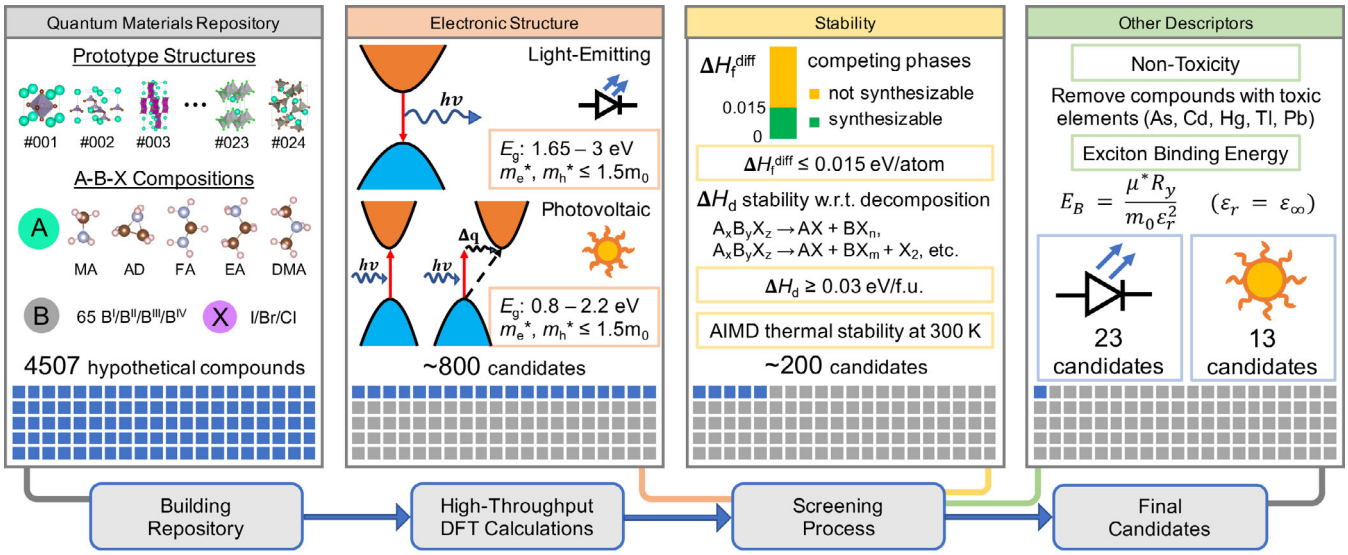

FIGURE 6 Schematic diagram of the high-throughput screening process. (Reprinted from Reference 69)

the compounds by comparing different crystal structures and M/M′ configurations. Second, they checked decomposition pathways and phase diagrams to screen the thermodynamic stability. Then, the optoelectronic properties of selected compounds were calculated. Finally, they explored octahedral tilting and its effects on the electronic properties of the compounds.

In 2019, our research group performed HT computational design of hybrid halide perovskites and perovskite derivatives for optoelectronics (Figure 6).[69] From AFLOWLIB and Materials Project, we first identified 24 prototype structures from existing ternary cesium metal halide compounds ($Cs_xB_yX_z$). Second, we generated 4,507 hypothetical organic–inorganic hybrid metal halide compounds ($A_xB_yX_z$), in which A can be five different organic cations, B can be 65 elements with oxidation states ranging from +1 to +4, and X can be I, Br, or Cl. Third, the 4,507 compounds were calculated in a high-throughput fashion. To discover materials with desired optoelectronic properties, we screened bandgap calculated at different PBE/HSE/SOC levels, effective masses, and exciton binding energy for different applications of photovoltaics and light-emitting, respectively. Thermodynamic stability was carefully assessed: we calculated decomposition enthalpy with respect to all possible decomposition pathways, and we considered candidates with the same composition and stoichiometry as competing phases. Room-temperature dynamic stability was evaluated using AIMD. Compounds containing toxic elements and traditional perovskites discovered before were excluded. In the end, we identified 29 candidates, among which 23 are for light-emitting applications and 13 are for photovoltaic applications. All the candidates are perovskite derivatives in five prototype structures, whose stoichiometry includes 2:1:4, 3:2:9, and 2:1:6, and they contain B-site elements with oxidation states from +2 to +4. More recently, we systematically studied the stability diagram, absorption coefficients, and defect tolerance as additional descriptors for the 29 candidates using high-throughput computation.[94] All candidates show a wide thermodynamically stable range for equilibrium growth, and most candidates have large averaged absorption coefficients at 450 nm. The defect tolerance, in specific, was determined by calculating about 5,000 neutral and charged defect structures, and 15 out of the 29 candidates show high defect tolerance.

3.5 | Incorporation of machine learning in HT computational design

Nowadays, machine learning (ML) sees its applications in materials science.[122–124] It is especially useful to deal with large-scale data and thus is often combined with HT computational design.[77,125] A common ML approach to materials discovery consists of the following steps. First, based on ML algorithms selected, ML model is trained on databases built from HT first-principles calculations. Like descriptors in HT computational design, features are important in the training of ML models. A successful ML model requires careful feature engineering. Then, the ML model predicts more materials outside the databases to circumvent further first-principles calculations. The ML model could also find

scientific trends and relationships between features and predicted properties. Compared to pure HT computation design, the incorporation of ML methods makes design processes more cost-effective, but it often leads to lower prediction accuracy. In this section, we review studies that combine the ML method with first-principles calculations to predict halide perovskite optoelectronic materials.

In 2018, Lu et al. combined ML techniques and density functional theory calculations to predict hybrid perovskite photovoltaics based on bandgap (Figure 7).[77] The authors first performed feature engineering and selected 14 most important features. Then, they trained their ML model on bandgaps of 212 reported halide perovskites and predicted 5,158 unexplored perovskites' bandgap values. The ML method also established the mapping of structure–property relationships for the bandgap. After screening predicted bandgap, six orthorhombic lead-free perovskites with proper bandgap and room-temperature stability were discovered out of 5,158 unexplored hybrid halide perovskites. Further, the authors performed DFT calculations on the six perovskites, including the electronic structure and thermal and environmental stability calculations. Finally, three $ASnBr_3$ perovskites were selected as final candidates, which show high stability and proper bandgaps. The approach greatly reduces time and cost for large-scale DFT calculations by the ML method, and only calculate the most promising candidates at DFT level.

In 2019, Im et al. applied the machine-learning algorithm of gradient-boosted regression trees (GBRT) to a calculated dataset of electronic structures for lead-free double perovskites for photovoltaics.[126] First, the authors calculated 540 hypothetical inorganic halide double perovskites $A_2B^{1+}B^{3+}X_6$ to generate a dataset including their formation enthalpy and bandgap values. Next, the authors applied the GBRT algorithm on the dataset and performed regression

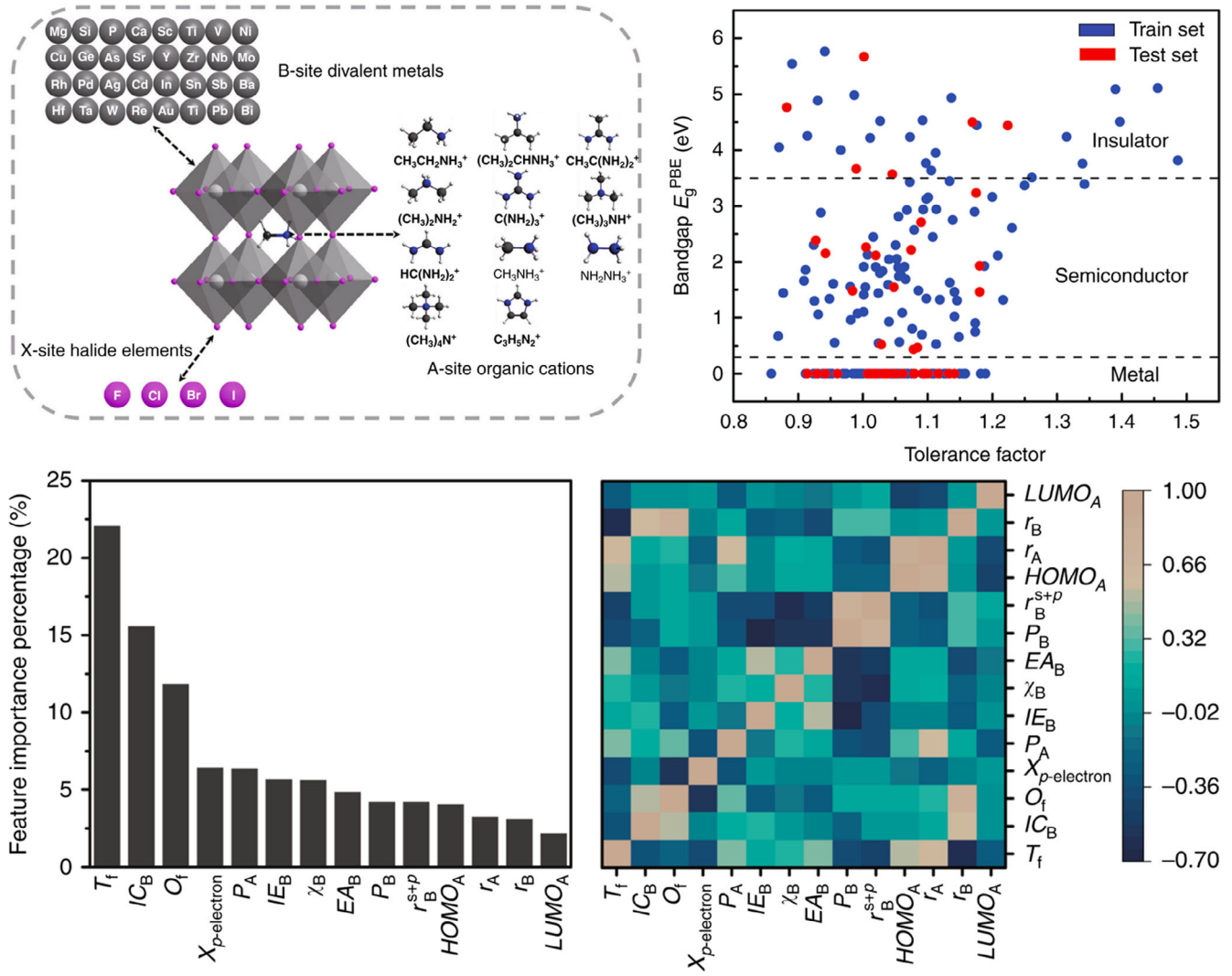

FIGURE 7 (Left) Input dataset of hybrid perovskites for training and testing and (right) importance and correlation of the selected features. (Reprinted from Reference 77)

to predict the values for halide double perovskites. The results show good averaged root-mean-square-error (RMSE) for formation enthalpy (0.021 eV/atom) and less-accurate results for bandgap (RMSE = 0.223 eV). The GBRT algorithm could also interpret the prediction results via feature importance scores, and determined that which five and seven features are the minimal sets to accurately predict formation enthalpy and bandgap, respectively.

In 2019, Li et al. reported a new way to determine the formability and stability of perovskites by combining high-throughput DFT calculations and ML methods.[125] In this work, the authors first established a database of calculated decomposition energies for 354 halide perovskite candidates. Then, they used the DFT-calculated database to train an ML model based on ionic radii as features. The ML model mapped the relationship between the ionic radii and the decomposition energies. Next, the authors validated the ML model independently by experimental results of 246 double perovskites. The ML model performed better than empirical descriptors like the tolerance factor. Finally, the authors used the ML model to predict decomposition energies for about 10,000 halide perovskite and mixed-halide perovskites.

In 2020, Saidi et al. developed a hierarchical ML model to predict the electronic properties of metal halide perovskites using convolutional neural networks (CNN).[127] Each neural network element is designated with a role from predicting features to narrowing down value ranges. In this study, the authors first calculated 862 ABX_3 perovskites to build a dataset containing their bandgap and structural parameters. The materials design space is created mainly by incorporating 18 A-site organic molecules. Then, the authors identified 29 elemental features, six precursor-based features, and two ABX_3 structure-based features. The features were engineered to determine the 11 most important features. Next, the authors trained a CNN using 80% of the dataset, and also applied a hierarchical CNN (HCNN) to address the imbalanced nature of the materials dataset. The lattice constant and octahedral tilt angle was found to be most important to develop a predictive model for the bandgap. Finally, the hierarchical ML model predicted the lattice constants, octahedral angle, and bandgap for metal halide perovskites with root-mean-square errors of 0.01 Å, 5°, and 0.02 eV, respectively. The hierarchical ML model showed high fidelity compared to straight-forward methods because it reduces issues caused by common imbalanced dataset distributions.

4 | SUMMARY AND OUTLOOK

In summary, we review recent research progress on the HT materials design of halide perovskites and beyond for optoelectronic applications, including the strategy of developing appropriate materials descriptors and the discovered candidate materials. Although many promising materials candidates have been predicted from these computational research work, additional efforts are still needed to examine their synthesizability, validate their properties, and realize optoelectronic devices based on these materials. In addition, next-step computational screening efforts could be done to explore novel materials structures and to further improve the efficiency of HT materials design, for example, using the emerging ML approach. Based on these considerations, we highlight possible future research directions as follows.

1. Stable and lead-free halide semiconductors that exhibit similar exceptional properties as lead halide perovskites could revolutionize many fields including the solar cell industry. Tables 1–4 summarize promising alternative materials to lead halide perovskites predicted from HT computational design, which can be classified into four categories. Generally, these materials need more detailed characterization and specific development for their applications in optoelectronic devices through additional experimental efforts, along with more accurate computational/theoretical studies. The IVA-element based single perovskites have been enumerated by early HT studies, and a large number of experiments have demonstrated their advantages and disadvantages (Table 1). Despite the elimination of toxicity in these perovskites, oxidation of divalent Ge or Sn ions poses ambient stability issues. For other element-based single perovskites, most search efforts considered various B-site cations solely with the perovskite structure and did not compare the candidates' stability or synthesizability with their competing phases in other possible structures. This leads to the fact that most predicted compositions crystallize in non-perovskite structures, and that the candidates do not have much experimental validation in Table 2. For double perovskites, because of the large chemical search space induced by their quaternary composition, there are much more prediction results than the other three categories of materials, and several predicted compounds have been successfully synthesized (Table 3). However, some predicted compounds like A_2GeSnX_6 double perovskites are less inspiring because they are simple combinations of IVA element-based single perovskites. In addition, some double perovskite predictions also have the problem of stability overestimation. One example is the predicted family of $A_2In(I)M(III)X_6$ (M = Bi, Sb) double perovskites. Theoretical and experimental studies proved that these perovskites are intrinsically unstable with respect to oxidation

TABLE 1 List of compounds in the search space of IVA element-based single perovskites designed from high-throughput computational studies reviewed in this article: compound, lattice system, space group, lattice parameters, bandgap, and experimental validation

Compound	Lattice system	Space group	Lattice parameters			E_g (eV)	Reference	Experimental validation
			a (Å)	*b* (Å)	*c* (Å)			
$RbSnBr_3$ ∘	Cubic	–	5.87	5.87	5.87	2.26	46	47
$CsSnBr_3$ ∘	Cubic	–	5.89	5.89	5.89	2.27	46	48
$CsGeI_3$ ∘	Cubic	–	5.99	5.99	5.99	1.93	46	49
$CsGeI_3$ ∘	Cubic	–	–	–	–	1.15	50	49
$CsGeBr_3$ ∘	Cubic	–	–	–	–	1.64	50	51
$HAGeBr_3$ ∘	Cubic	–	–	–	–	2.26	50	–
$DAGeBr_3$ ∘	Cubic	–	–	–	–	2.47	50	–
$MAGeI_3$ ∘	Cubic	–	6.10	6.10	6.10	1.98	50	–
$CsSnI_3$ ∘	Cubic	–	–	–	–	0.95	50	52,53
$CsSnBr_3$ ∘	Cubic	–	–	–	–	1.53	50	48
$CsSnCl_3$ ∘	Cubic	–	–	–	–	2.14	50	54
$MASnI_3$ ∘	Cubic	–	6.26	6.26	6.26	1.26	50	52,55,56
$MASnBr_3$ ∘	Cubic	–	–	–	–	2.00	50	56
$FASnI_3$ ∘	Cubic	–	–	–	–	1.21	50	52,57
$EASnI_3$ ∘	Cubic	–	–	–	–	1.70	50	–
$GASnI_3$ ∘	Cubic	–	–	–	–	1.78	50	–
$DEASnI_3$ ∘	Cubic	–	–	–	–	1.62	50	–
$CsSnI_3$ ∘	–	–	–	–	–	0.95	58	52,53
$FASnI_3$ ∘	–	–	–	–	–	1.00	58	52,57
$CsSnBr_3$ ∘	–	–	–	–	–	1.07	58	48
$CsGeI_3$ ∘	–	–	–	–	–	1.28	58	49
$MASnI_3$ ∘	–	–	–	–	–	1.43	58	52,55,56
$CsGeBr_3$ ∘	–	–	–	–	–	1.56	58	51
$MAGeI_3$ ∘	–	–	–	–	–	1.83	58	–
$MASnBr_3$ ∘	–	–	–	–	–	1.89	58	56
$MASiI_3$ ∘	–	–	–	–	–	1.44	58	–
$MA_{0.75}Cs_{0.25}SnI_3$ ∘	–	–	–	–	–	1.20	59	–
$MA_{0.875}Cs_{0.125}SnI_3$ ∘	–	–	–	–	–	1.18	59	–
$MA_{0.75}Rb_{0.25}SnI_3$ ∘	–	–	–	–	–	1.21	59	–
$FA_{0.5}Cs_{0.5}SnI_3$ ∘	–	–	–	–	–	1.11	59	–
$FA_{0.5}Rb_{0.5}SnI_3$ ∘	–	–	–	–	–	1.12	59	–

Note: In this and the following tables: Symbols following compound formulas denote the specific optoelectronic applications predicted: circles (∘) denote photovoltaic applications, triangles (△) denote light-emitting applications, and no symbol means that the prediction was targeted for general optoelectronic applications. The lattice system and space group of most compounds refer to their assumed structures (starting from which the compounds were constructed), and their optimized structures do not always strictly belong to the same lattice system and space group, especially for organic–inorganic hybrid compounds. For lattice parameters and bandgap, the values calculated at the highest or most accurate level of theory in the reference are shown here. The experimental validation is not an exhaustive list. Note that, for each compound, synthesis of its structural isomer (having the same chemical formula but different structures) is not considered as its experimental validation.

into In(III)-based compounds and that the HT predictions neglected redox reactions as decomposition pathways.[71] Another example is the HT prediction of Cu(I)-based double perovskites. Indeed, Cu(I) atoms tend to form [CuX_4]

TABLE 2 List of compounds in the search space of other element-based single perovskites designed from high-throughput computational studies reviewed in this article

			Lattice parameters					
Compound	**Lattice system**	**Space group**	***a* (Å)**	***b* (Å)**	***c* (Å)**	**E_g (eV)**	**Ref**	**Experimental validation**
$CsMgI_3$ ∘	[a]	–	–	–	–	[b]	78	–
$CsVI_3$ ∘	[a]	–	–	–	–	[b]	78	–
$CsMnI_3$ ∘	[a]	–	–	–	–	[b]	78	–
$CsMnBr_3$ ∘	[a]	–	–	–	–	[b]	78	–
$CsNiBr_3$ ∘	[a]	–	–	–	–	[b]	78	–
$CsNiCl_3$ ∘	[a]	–	–	–	–	[b]	78	–
$CsCdI_3$ ∘	[a]	–	–	–	–	[b]	78	–
$CsCdBr_3$ ∘	[a]	–	–	–	–	[b]	78	–
$CsCdCl_3$ ∘	[a]	–	–	–	–	[b]	78	–
$CsHgBr_3$ ∘	[a]	–	–	–	–	[b]	78	–
$CsHgCl_3$ ∘	[a]	–	–	–	–	[b]	78	–
$CsHgF_3$ ∘	[a]	–	–	–	–	[b]	78	–
$CsGaCl_3$ ∘	[a]	–	–	–	–	[b]	78	–
$CsInBr_3$ ∘	[a]	–	–	–	–	[b]	78	79
$CsInCl_3$ ∘	[a]	–	–	–	–	[b]	78	79
$MACa_{0.5}Si_{0.5}I_3$ ∘	Tetragonal	I4/mcm	12.2	12.4	12.3	1.33	80	–
$MACa_{0.125}Si_{0.875}I_3$ ∘	Tetragonal	I4/mcm	12.1	12.6	12.5	1.54	80	–
$MAZn_{0.5}Si_{0.5}I_3$ ∘	Tetragonal	I4/mcm	12.4	12.9	12.7	1.89	80	–
$MAAuI_3$ ∘	–	–	–	–	–	1.34	58	81
$FAAuI_3$ ∘	–	–	–	–	–	1.38	58	81
$MAAuBr_3$ ∘	–	–	–	–	–	1.39	58	–
$KFeI_3$ ∘	–	–	–	–	–	1.64	59	–
$CsMn_{0.875}Fe_{0.125}I_3$ ∘	–	–	–	–	–	1.33	59	–
$CsMn_{0.75}Co_{0.25}I_3$ ∘	–	–	–	–	–	1.50	59	–
$MA_{0.5}Cs_{0.5}MnI_3$ ∘	–	–	–	–	–	1.44	59	–

Note: For each other element-based single perovskite compound, experimental validation of its analogs with different A-site cations is also included.
[a]The structural optimization started from five unique orthorhombic perovskite unit cells, and the resulting structures were not disclosed in reference.
[b]The bandgaps were given in color maps without explicit values.

tetrahedral instead of [CuX_6] octahedral as in perovskite structures, as proved by theoretical and experimental efforts.[72] Notably, there is a special class of materials called mixed-valence perovskites (e.g., In(I)–In(III) and Au(I)–Au(III) perovskites). These perovskites have ternary compositions of single perovskites but the +1/+3 valence states of metal ions in double perovskites. Although predicted by HT studies, In(I)–In(III) perovskites have the same chemical stability problem of In(I) oxidation as in In(I)-based double perovskites. A later computational study also showed that they have indirect and too small bandgaps, and that local mixed-valence In(I)–In(III) configuration in In(I)–Bi(III) double perovskites induces deep defect states.[128] Similarly, another study showed that the predicted Au(I)–Au(III) perovskites have two-dimensional electronic properties including highly anisotropic band structures and flat conduction band and valence band at the band edges.[129]

TABLE 3 List of compounds in the search space of double perovskites designed from high-throughput computational studies reviewed in this article

Compound	Lattice system	Space group	Lattice parameters			E_g (eV)	Ref	Experimental validation
			a (Å)	*b* (Å)	*c* (Å)			
$Cs_2CuSbCl_6$ ◦	Cubic	$Fm\bar{3}m$	10.52	10.52	10.52	1.82	70	⊗[72]
$Cs_2CuSbBr_6$ ◦	Cubic	$Fm\bar{3}m$	11.07	11.07	11.07	1.24	70	⊗[72]
$Cs_2CuBiBr_6$ ◦	Cubic	$Fm\bar{3}m$	11.17	11.17	11.17	1.51	70	⊗[72]
$Cs_2AgSbBr_6$ ◦	Cubic	$Fm\bar{3}m$	11.37	11.37	11.37	1.67	70	103
Cs_2AgSbI_6 ◦	Cubic	$Fm\bar{3}m$	12.13	12.13	12.13	0.95	70	104
Cs_2AgBiI_6 ◦	Cubic	$Fm\bar{3}m$	12.24	12.24	12.24	1.32	70	105,106
$Cs_2AuSbCl_6$ ◦	Cubic	$Fm\bar{3}m$	10.83	10.83	10.83	1.05	70	–
$Cs_2AuBiCl_6$ ◦	Cubic	$Fm\bar{3}m$	10.94	10.94	10.94	1.38	70	–
$Cs_2AuBiBr_6$ ◦	Cubic	$Fm\bar{3}m$	11.42	11.42	11.42	0.84	70	–
$Cs_2InSbCl_6$ ◦	Cubic	$Fm\bar{3}m$	11.32	11.32	11.32	1.02	70	⊗[71]
$Cs_2InBiCl_6$ ◦	Cubic	$Fm\bar{3}m$	11.44	11.44	11.44	0.91	70	⊗[71]
$Cs_2AgInBr_6$ ◦	Cubic	$Fm\bar{3}m$	11.156	11.156	11.156	1.5	107	108
$Rb_2AgInBr_6$ ◦	Cubic	$Fm\bar{3}m$	11.064	11.064	11.064	1.46	107	108
$Rb_2CuInCl_6$ ◦	Cubic	$Fm\bar{3}m$	10.237	10.237	10.237	1.36	107	⊗[72]
$Cs_2BiAg_{0.875}Cu_{0.125}Cl_6$ ◦	Cubic	$Fm\bar{3}m$	–	–	–	1.9	74	–
$Cs_2BiAg_{0.75}Cu_{0.25}Cl_6$ ◦	Cubic	$Fm\bar{3}m$	–	–	–	1.6	74	–
$Cs_2AgInBr_6$ ◦	Cubic	$Fm\bar{3}m$	11.16	11.16	11.16	1.49	60	108
$Cs_2InAsBr_6$ ◦	Cubic	$Fm\bar{3}m$	11.43	11.43	11.43	0.36	60	–
$Cs_2InBiCl_6$ ◦	Cubic	$Fm\bar{3}m$	11.42	11.42	11.42	0.92	60	⊗[71]
$Cs_2InBiBr_6$ ◦	Cubic	$Fm\bar{3}m$	11.89	11.89	11.89	0.29	60	⊗[71]
$Cs_2InSbBr_6$ ◦	Cubic	$Fm\bar{3}m$	11.76	11.76	11.76	0.33	60	⊗[71]
$Cs_2TlAsBr_6$ ◦	Cubic	$Fm\bar{3}m$	11.58	11.58	11.58	1.23	60	–
Cs_2TlAsI_6 ◦	Cubic	$Fm\bar{3}m$	12.34	12.34	12.34	0.79	60	–
$Cs_2TlSbBr_6$ ◦	Cubic	$Fm\bar{3}m$	11.90	11.90	11.90	1.11	60	–
Cs_2InGaI_6 ◦	Cubic	$Fm\bar{3}m$	12.14	12.14	12.14	0.76	60	–
$Cs_2InInBr_6$ ◦	Cubic	$Fm\bar{3}m$	11.63	11.63	11.63	1.57	60	–
$Cs_2TlTlBr_6$ ◦	Cubic	$Fm\bar{3}m$	11.74	11.74	11.74	1.07	60	–
$Cs_2NaMnCl_6$	Cubic	$Fm\bar{3}m$	–	–	–	2.69/2.96*	61	–
Cs_2KMnCl_6	Cubic	$Fm\bar{3}m$	–	–	–	3.30/3.30*	61	–
$Cs_2NaNiCl_6$	Cubic	$Fm\bar{3}m$	–	–	–	1.78/2.08*	61	–
Cs_2KNiCl_6	Cubic	$Fm\bar{3}m$	–	–	–	2.44/2.48*	61	–
Cs_2GeSnI_6 ◦	–	–	–	–	–	1.04	58	–
MA_2SiSnI_6 ◦	–	–	–	–	–	1.22	58	–
FA_2GeSnI_6 ◦	–	–	–	–	–	1.24	58	–
$Cs_2GeSnBr_6$ ◦	–	–	–	–	–	1.29	58	–
MA_2GeSnI_6 ◦	–	–	–	–	–	1.56	58	–
FA_2SiGeI_6 ◦	–	–	–	–	–	1.66	58	–
MA_2SiGeI_6 ◦	–	–	–	–	–	1.82	58	–
MA_2InBiI_6 ◦	–	–	–	–	–	0.88	58	⊗[71]
MA_2InSbI_6 ◦	–	–	–	–	–	1.01	58	⊗[71]
FA_2GaBiI_6 ◦	–	–	–	–	–	1.10	58	–

(Continues)

TABLE 3 (Continued)

Compound	Lattice system	Space group	Lattice parameters			E_g (eV)	Ref	Experimental validation
			a (Å)	*b* (Å)	*c* (Å)			
MA_2GaBiI_6 ∘	–	–	–	–	–	1.16	[58]	–
$MA_2InBiBr_6$ ∘	–	–	–	–	–	1.18	[58]	⊗[71]
FA_2InBiI_6 ∘	–	–	–	–	–	1.19	[58]	⊗[71]
MA_2GaSbI_6 ∘	–	–	–	–	–	1.21	[58]	–
Cs_2GaBiI_6 ∘	–	–	–	–	–	1.21	[58]	–
$Cs_2GaBiBr_6$ ∘	–	–	–	–	–	1.29	[58]	–
$MA_2InSbBr_6$ ∘	–	–	–	–	–	1.29	[58]	⊗[71]
$Cs_2GaBiCl_6$ ∘	–	–	–	–	–	1.39	[58]	–
$Cs_2GaSbCl_6$ ∘	–	–	–	–	–	1.43	[58]	–
$Cs_2InBiBr_6$ ∘	–	–	–	–	–	1.45	[58]	⊗[71]
MA_2GaPBr_6 ∘	–	–	–	–	–	1.64	[58]	–
$MA_2GaBiBr_6$ ∘	–	–	–	–	–	1.72	[58]	–
$MA_2GaSbBr_6$ ∘	–	–	–	–	–	1.77	[58]	–
$MA_2AgAuBr_6$ ∘	–	–	–	–	–	1.27	[58]	–
$MA_2CuAuBr_6$ ∘	–	–	–	–	–	1.29	[58]	⊗[72]
MA_2CuAuI_6 ∘	–	–	–	–	–	1.30	[58]	⊗[72]
FA_2AgAuI_6 ∘	–	–	–	–	–	1.35	[58]	–
Cs_2RhInI_6 ∘	–	–	–	–	–	1.42	[58]	–
FA_2RhInI_6 ∘	–	–	–	–	–	1.63	[58]	–
MA_2RhGaI_6 ∘	–	–	–	–	–	1.67	[58]	–
Cs_2RhGaI_6 ∘	–	–	–	–	–	1.68	[58]	–
$Cs_2RhInBr_6$ ∘	–	–	–	–	–	1.76	[58]	–
$MA_2RhInBr_6$ ∘	–	–	–	–	–	1.83	[58]	–
MA_2CuInI_6 ∘	–	–	–	–	–	1.29	[58]	⊗[72]
FA_2AuGaI_6 ∘	–	–	–	–	–	1.44	[58]	–
MA_2AuInI_6 ∘	–	–	–	–	–	1.47	[58]	–
MA_2AuGaI_6 ∘	–	–	–	–	–	1.50	[58]	–
MA_2AgBiI_6 ∘	–	–	–	–	–	2.09	[58]	–
MA_2CuBiI_6 ∘	–	–	–	–	–	2.11	[58]	⊗[72]
$DMAAg_{0.5}Bi_{0.5}I_3$ ∘	–	–	–	–	–	1.53	[59]	105,106
$FAAg_{0.5}Sb_{0.5}Br_3$ ∘	–	–	–	–	–	1.56	[59]	103

Note: For each double perovskite compound, experimental validation of its analogues with different A-site cations is also included. ⊗ denotes negative experimental validation. * denotes that the bandgaps were calculated for two different antiferromagnetic spin states.

2. As large-scale materials data have been generated from the HT studies, screening of candidates for other optoelectronic applications, including transistors, lasers, and wide-bandgap top-cell materials in perovskite–silicon tandem solar cells, can be achieved with a reduced computational cost. These materials data also enable the training of ML algorithms to reveal the undiscovered trends and materials design principles for halide optoelectronics.
3. HT computational design based on perovskite-derived structures is a promising direction and have started lately. These structures could show intrinsically higher thermodynamic stability than perovskite structures. Besides the single-perovskite derivatives reviewed, there are still many versatile prototype structures such as double perovskites and low-dimensional perovskites. The prior materials design in these perovskite-derived structures has been proven

TABLE 4 List of compounds in the search space of perovskite derivatives designed from high-throughput computational studies reviewed in this article

Compound	Lattice system	Space group	Lattice parameters			E_g (eV)	Ref	Experimental validation
			a (Å)	*b* (Å)	*c* (Å)			
$RbSbI_4$	Rhombohedral	R3c	–	–	–	2.34	111	–
$CsSbI_4$	Rhombohedral	R3c	–	–	–	2.34	111	–
$K_3Sb_2I_9$	Hexagonal	$P\bar{3}m1$	–	–	–	2.04	111	112
$Rb_3Sb_2I_9$	Hexagonal	$P\bar{3}m1$	–	–	–	2.07	111	112
$Cs_3Sb_2I_9$	Hexagonal	$P\bar{3}m1$	–	–	–	2.13	111	112
$Rb_3In_2I_9$	Hexagonal	$P6_3/mmc$	–	–	–	2.05	111	–
$Cs_3In_2I_9$	Hexagonal	$P6_3/mmc$	–	–	–	2.12	111	–
$Cs_3Ga_2I_9$	Hexagonal	$P6_3/mmc$	–	–	–	1.72	111	–
$Cs_4SnSb_2I_{12}$ ∘	Monoclinic	C2/m	8.72	8.72	15.13	1.50	113	–
$Cs_4GeSb_2I_{12}$ ∘	Monoclinic	C2/m	8.61	8.61	14.93	1.60	113	–
$K_4SnSb_2Cl_{12}$	Monoclinic	C2/m	–	–	–	2.63	114	–
$K_4SnBi_2Cl_{12}$	Monoclinic	C2/m	–	–	–	2.54	114	–
$K_4SnSb_2Br_{12}$	Monoclinic	C2/m	–	–	–	2.17	114	–
$Rb_4SnSb_2Cl_{12}$	Monoclinic	C2/m	–	–	–	2.45	114	–
$Rb_4SnBi_2Cl_{12}$	Monoclinic	C2/m	–	–	–	2.43	114	–
$Rb_4SnSb_2Br_{12}$	Monoclinic	C2/m	–	–	–	2.07	114	–
MA_2GeBr_4 △	Tetragonal	I4/mmm	5.54	5.54	19.02	1.99	69,94	–
MA_2GeI_4 ∘△	Tetragonal	I4/mmm	5.94	5.87	20.11	1.66	69,94	–
MA_2SnCl_4 △	Tetragonal	I4/mmm	5.56	5.48	18.35	2.49	69,94	–
MA_2SnBr_4 ∘△	Tetragonal	I4/mmm	5.72	5.74	19.08	1.67	69,94	–
MA_2SnI_4 ∘	Tetragonal	I4/mmm	6.12	6.11	20.00	1.42	69,94	–
FA_2SnBr_4 ∘△	Tetragonal	I4/mmm	5.64	5.71	20.60	1.69	69,94	–
AD_2GeI_4 △	Tetragonal	I4/mmm	6.14	6.16	18.97	2.30	69,94	–
AD_2SnBr_4 △	Tetragonal	I4/mmm	5.87	5.86	18.09	2.51	69,94	–
AD_2SnI_4 ∘△	Tetragonal	I4/mmm	6.22	6.21	19.17	1.87	69,94	–
$MA_3In_2I_9$ △	Hexagonal	$P\bar{3}m1$	8.23	8.31	11.00	2.18	69,94	–
$MA_3Sb_2Br_9$ △	Hexagonal	$P\bar{3}m1$	7.71	7.71	10.37	2.70	69,94	–
$MA_3Sb_2I_9$ ∘△	Hexagonal	$P\bar{3}m1$	8.26	8.26	10.91	2.02	69,94	115,116
$MA_3Bi_2I_9$ ∘	Hexagonal	$P\bar{3}m1$	8.35	8.35	11.00	1.82	69,94	–
$FA_3Ga_2I_9$ △	Hexagonal	$P\bar{3}m1$	7.94	8.25	11.83	2.17	69,94	–
$FA_3In_2Br_9$ △	Hexagonal	$P\bar{3}m1$	7.38	7.83	11.17	2.91	69,94	–
$FA_3In_2I_9$ △	Hexagonal	$P\bar{3}m1$	8.04	8.30	11.67	1.90	69,94	–
$FA_3Bi_2I_9$ ∘△	Hexagonal	$P\bar{3}m1$	8.06	8.36	11.60	1.80	69,94	117
$AD_3Sb_2Br_9$ △	Hexagonal	$P\bar{3}m1$	8.30	8.36	9.55	2.52	69,94	–
$AD_3Sb_2I_9$ ∘△	Hexagonal	$P\bar{3}m1$	8.69	8.77	10.20	1.91	69,94	115,116
$AD_3Bi_2I_9$ ∘	Hexagonal	$P\bar{3}m1$	8.78	8.84	10.26	1.80	69,94	–
$FA_3Sb_2I_9$ △	Hexagonal	$P6_3/mmc$	8.02	8.32	23.18	2.54	69,94	118,119
$AD_3In_2I_9$ △	Hexagonal	$P6_3/mmc$	8.61	8.71	20.54	2.00	69,94	–
MA_2ZrI_6 △	Tetragonal	I4/mmm	8.18	8.19	12.37	2.60	69,94	–
AD_2HfI_6 △	Tetragonal	I4/mmm	8.47	8.46	12.17	2.89	69,94	–
AD_2SnBr_6 △	Tetragonal	I4/mmm	8.13	8.12	11.56	2.42	69,94	–

(Continues)

TABLE 4 (Continued)

Compound	Lattice system	Space group	Lattice parameters			E_g (eV)	Ref	Experimental validation
			a (Å)	*b* (Å)	*c* (Å)			
AD_2TeBr_6 △	Tetragonal	I4/mmm	8.29	8.30	11.18	2.71	69,94	–
MA_2SnI_6 ◦	Cubic	$Fm\bar{3}m$	11.61	11.44	12.55	0.80	69,94	120,121
MA_2TeI_6 ◦	Cubic	$Fm\bar{3}m$	11.67	11.51	12.58	1.77	69,94	120
AD_2TeI_6 ◦	Cubic	$Fm\bar{3}m$	12.54	11.63	12.17	1.87	69,94	–

Note: For each perovskite-derived compound, experimental validation of its analogs with different A-site cations is also included.

successful from the experimental synthesis of some candidate materials (Table 4). Also, an appropriate application of ML approach in these novel structures could further speed up the materials discovery process. However, it is noted that most ML models in the reviewed topic deal with perovskites only, and features that effectively account for different structures are scarce, and the inclusion of various prototype structures in the ML approach could be challenging but also interesting.

4. Although HT computational design is a powerful tool to discover novel materials at low cost, unreasonable process design (e.g., calculations of redundant materials that can be pre-excluded by basic chemical rules) may result in an unnecessary cost of computation resources and ineffective prediction results. As more and more HT materials screening studies become available for perovskite-related optoelectronics, some general protocols that regulate the methodologies, levels of theory, and the examination of materials stability should be considered. These protocols are important for the robustness and reliability of the screening results and more informative for guiding experimental studies. For example, as an essential property in computational prediction, thermodynamic stability should be rigorously analyzed by calculating decomposition enthalpy with respect to all possible pathways or by analyzing energy above the convex hull with phase diagrams. The ongoing development of automation toolkit and standard materials libraries will also greatly help apply such protocols in the HT studies.

ACKNOWLEDGMENT

This work was supported by Academic Senate General Campus Research Grant Committee at University of California San Diego and National Science Foundation under award number ACI-1550404.

AUTHOR CONTRIBUTIONS

Yuheng Li: Investigation; writing-original draft. **Kesong Yang:** Investigation; project administration; writing-review and editing.

CONFLICT OF INTEREST

The authors have declared no conflicts of interest for this article.

ORCID

Yuheng Li https://orcid.org/0000-0002-1865-1122
Kesong Yang https://orcid.org/0000-0002-9691-0636

RELATED WIREs ARTICLES

High-throughput computational screening of layered and two-dimensional materials

REFERENCES

1. Kojima A, Teshima K, Shirai Y, Miyasaka T. Organometal halide perovskites as visible-light sensitizers for photovoltaic cells. *J Am Chem Soc*. 2009;*131*:6050–6051.
2. Jeon NJ, Noh JH, Yang WS, et al. Compositional engineering of perovskite materials for high-performance solar cells. *Nature*. 2015; *517*:476–480.

3. McMeekin DP, Sadoughi G, Rehman W, et al. A mixed-cation lead mixed-halide perovskite absorber for tandem solar cells. *Science*. 2016;*351*:151–155.
4. Zhou H, Chen Q, Li G, et al. Interface engineering of highly efficient perovskite solar cells. *Science*. 2014;*345*:542–546.
5. Chen Y, Lei Y, Li Y, et al. Strain engineering and epitaxial stabilization of halide perovskites. *Nature*. 2020;*577*:209–215.
6. Veldhuis SA, Boix PP, Yantara N, et al. Perovskite materials for light-emitting diodes and lasers. *Adv Mater*. 2016;*28*:6804–6834.
7. NREL. Best Research-Cell Efficiency Chart; 2020. [Online; accessed April 8, 2020]. Available from: https://www.nrel.gov/pv/assets/pdfs/best-research-cell-efficiencies.20200311.pdf.
8. Grätzel M. The light and shade of perovskite solar cells. *Nat Mater*. 2014;*13*:838–842.
9. Jena AK, Kulkarni A, Miyasaka T. Halide perovskite photovoltaics: background, status, and future prospects. *Chem Rev*. 2019;*119*:3036–3103.
10. Dong Q, Fang Y, Shao Y, et al. Electron-hole diffusion lengths > 175 μm in solution-grown $CH_3NH_3PbI_3$ single crystals. *Science*. 2015;*347*:967–970.
11. Xing G, Mathews N, Sun S, et al. Long-range balanced electron- and hole-transport lengths in organic–inorganic $CH_3NH_3PbI_3$. *Science*. 2013;*342*:344–347.
12. Wehrenfennig C, Eperon GE, Johnston MB, Snaith HJ, Herz LM. High charge carrier mobilities and lifetimes in organolead trihalide perovskites. *Adv Mater*. 2014;*26*:1584–1589.
13. Li Y, Behtash M, Wong J, Yang K. Enhancing ferroelectric dipole ordering in organic-inorganic hybrid perovskite $CH_3NH_3PbI_3$: strain and doping engineering. *J Phys Chem C*. 2018;*122*:177–184.
14. Yin WJ, Shi T, Yan Y. Unusual defect physics in $CH_3NH_3PbI_3$ perovskite solar cell absorber. *Appl Phys Lett*. 2014;*104*:063903.
15. Walsh A, Scanlon DO, Chen S, Gong X, Wei SH. Self-regulation mechanism for charged point defects in hybrid halide perovskites. *Angew Chem Int Ed*. 2015;*54*:1791–1794.
16. Barrows AT, Pearson AJ, Kwak CK, Dunbar AD, Buckley AR, Lidzey DG. Efficient planar heterojunction mixed-halide perovskite solar cells deposited via spray-deposition. *Energ Environ Sci*. 2014;*7*:2944–2950.
17. Bryant D, Aristidou N, Pont S, et al. Light and oxygen induced degradation limits the operational stability of methylammonium lead triiodide perovskite solar cells. *Energ Environ Sci*. 2016;*9*:1655–1660.
18. Conings B, Drijkoningen J, Gauquelin N, et al. Intrinsic thermal instability of methylammonium lead trihalide perovskite. *Adv Energy Mater*. 2015;*5*:1500477.
19. Giustino F, Snaith HJ. Toward lead-free perovskite solar cells. *ACS Energy Lett*. 2016;*1*:1233–1240.
20. Chakraborty S, Xie W, Mathews N, et al. Rational design: a high-throughput computational screening and experimental validation methodology for lead-free and emergent hybrid perovskites. *ACS Energy Lett*. 2017;*2*:837–845.
21. Huo C, Cai B, Yuan Z, Ma B, Zeng H. Two-dimensional metal halide perovskites: theory, synthesis, and optoelectronics. *Small Methods*. 2017;*1*:1600018.
22. Jodlowski A, Rodríguez-Padrón D, Luque R, de Miguel G. Alternative perovskites for photovoltaics. *Adv Energy Mater*. 2018;*8*:1703120.
23. Xu Q, Yang D, Lv J, Sun YY, Zhang L. Perovskite solar absorbers: materials by design. *Small Methods*. 2018;*2*:1700316.
24. Zhao XG, Yang D, Ren JC, Sun Y, Xiao Z, Zhang L. Rational design of halide double perovskites for optoelectronic applications. *Joule*. 2018;*2*:1662–1673.
25. Xiao Z, Song Z, Yan Y. From lead halide perovskites to lead-free metal halide perovskites and perovskite derivatives. *Adv Mater*. 2019;*31*:1803792.
26. Greeley J, Jaramillo TF, Bonde J, Chorkendorff I, Norskov JK. Computational high-throughput screening of electrocatalytic materials for hydrogen evolution. *Nat Mater*. 2006;*5*:909–913.
27. Ceder G. Opportunities and challenges for first-principles materials design and applications to Li battery materials. *MRS Bull*. 2010;*35*:693–701.
28. Wang S, Wang Z, Setyawan W, Mingo N, Curtarolo S. Assessing the thermoelectric properties of sintered compounds via high-throughput *Ab-Initio* calculations. *Phys Rev X*. 2011;*1*:021012.
29. Armiento R, Kozinsky B, Fornari M, Ceder G. Screening for high-performance piezoelectrics using high-throughput density functional theory. *Phys Rev B*. 2011;*84*:014103.
30. Yang K, Setyawan W, Wang S, Nardelli MB, Curtarolo S. A search model for topological insulators with high-throughput robustness descriptors. *Nat Mater*. 2012;*11*:614–619.
31. Curtarolo S, Hart GLW, Nardelli MB, Mingo N, Sanvito S, Levy O. The high-throughput highway to computational materials design. *Nat Mater*. 2013;*12*:191–201.
32. Armiento R, Kozinsky B, Hautier G, Fornari M, Ceder G. High-throughput screening of perovskite alloys for piezoelectric performance and thermodynamic stability. *Phys Rev B*. 2014;*89*:134103.
33. Gautier R, Zhang X, Hu L, et al. Prediction and accelerated laboratory discovery of previously unknown 18-electron ABX compounds. *Nat Chem*. 2015;*7*:308–316.
34. Brunin G, Ricci F, Ha VA, Rignanese GM, Hautier G. Transparent conducting materials discovery using high-throughput computing. *NPJ Comput Mater*. 2019;*5*:63.
35. Sanvito S, Oses C, Xue J, et al. Accelerated discovery of new magnets in the Heusler alloy family. *Sci Adv*. 2017;*3*:e1602241.
36. Yang K, Nazir S, Behtash M, Cheng J. High-throughput design of two-dimensional electron gas systems based on polar/nonpolar perovskite oxide heterostructures. *Sci Rep*. 2016;*6*:34667.

37. Yang K. High-throughput design of functional materials using materials genome approach. *Chin Phys B*. 2018;*27*:128103.
38. Cheng J, Yang K. Design of two-dimensional electron gas systems via polarization discontinuity from large-scale first-principles calculations. *J Mater Chem C*. 2018;*6*:6680–6690.
39. Curtarolo S, Setyawan W, Wang S, et al. AFLOWLIB.ORG: a distributed materials properties repository from high-throughput *ab Initio* calculations. *Comput Mater Sci*. 2012;*58*:227–235.
40. Ong SP, Richards WD, Jain A, et al. Python materials genomics (pymatgen): a robust, open-source python library for materials analysis. *Comput Mater Sci*. 2013;*68*:314–319.
41. Larsen AH, Mortensen JJ, Blomqvist J, et al. The atomic simulation environment—a python library for working with atoms. *J Phys Condens Matter*. 2017;*29*:273002.
42. Yang X, Wang Z, Zhao X, Song J, Zhang M, Liu H. MatCloud: a high-throughput computational infrastructure for integrated management of materials simulation, data and resources. *Comput Mater Sci*. 2018;*146*:319–333.
43. Jain A, Ong SP, Hautier G, et al. Commentary: The materials project: a materials genome approach to accelerating materials innovation. *APL Mater*. 2013;*1*:011002.
44. Saal JE, Kirklin S, Aykol M, Meredig B, Wolverton C. Materials design and discovery with high-throughput density functional theory: the open quantum materials database (OQMD). *JOM*. 2013;*65*:1501–1509.
45. Landis DD, Hummelshoj JS, Nestorov S, et al. The computational materials repository. *Comput Sci Eng*. 2012;*14*:51–57.
46. Krishnamoorthy T, Ding H, Yan C, et al. Lead-free germanium iodide perovskite materials for photovoltaic applications. *J Mater Chem A*. 2015;*3*:23829–23832.
47. Kuok M, Tan L, Shen Z, Huan C, Mok K. A Raman study of $RbSnBr_3$. *Solid State Commun*. 1996;*97*:497–501.
48. Fabini DH, Laurita G, Bechtel JS, et al. Dynamic Stereochemical activity of the Sn^{2+} lone pair in perovskite $CsSnBr_3$. *J Am Chem Soc*. 2016;*138*:11820–11832.
49. Wu X, Song W, Li Q, Zhao X, He D, Quan Z. Synthesis of lead-free $CsGeI_3$ perovskite colloidal nanocrystals and electron beam-induced transformations. *Chem Asian J*. 2018;*13*:1654–1659.
50. Yang D, Lv J, Zhao X, et al. Functionality-directed screening of Pb-free hybrid organic–inorganic perovskites with desired intrinsic photovoltaic functionalities. *Chem Mater*. 2017;*29*:524–538.
51. Tang LC, Huang JY, Chang C, Lee M, Liu L. New infrared nonlinear optical crystal $CsGeBr_3$: synthesis, structure and powder second-harmonic generation properties. *J Phys Condens Matter*. 2005;*17*:7275–7286.
52. Stoumpos CC, Malliakas CD, Kanatzidis MG. Semiconducting tin and lead iodide perovskites with organic cations: phase transitions, high mobilities, and near-infrared Photoluminescent properties. *Inorg Chem*. 2013;*52*:9019–9038.
53. Kumar MH, Dharani S, Leong WL, et al. Lead-free halide perovskite solar cells with high photocurrents realized through vacancy modulation. *Adv Mater*. 2014;*26*:7122–7127.
54. Sharma S, Weiden N, Weiss A. Phase transitions in $CsSnCl_3$ and $CsPbBr_3$ an NMR and NQR study. *Z Naturforsch A*. 1991;*46*:329–336.
55. Noel NK, Stranks SD, Abate A, et al. Lead-free organic–inorganic tin halide Perovskites for photovoltaic applications. *Energ Environ Sci*. 2014;*7*:3061–3068.
56. Hao F, Stoumpos CC, Cao DH, Chang RP, Kanatzidis MG. Lead-free solid-state organic–inorganic halide perovskite solar cells. *Nat Photon*. 2014;*8*:489–494.
57. Liao W, Zhao D, Yu Y, et al. Fabrication of efficient low-bandgap perovskite solar cells by combining formamidinium tin iodide with methylammonium lead iodide. *J Am Chem Soc*. 2016;*138*:12360–12363.
58. Nakajima T, Sawada K. Discovery of Pb-free perovskite solar cells via high-throughput simulation on the K computer. *J Phys Chem Lett*. 2017;*8*:4826–4831.
59. Jacobs R, Luo G, Morgan D. Materials discovery of stable and nontoxic halide perovskite materials for high-efficiency solar cells. *Adv Funct Mater*. 2019;*29*:1804354.
60. Cai Y, Xie W, Teng YT, et al. High-throughput computational study of halide double perovskite inorganic compounds. *Chem Mater*. 2019;*31*:5392–5401.
61. Bartel CJ, Clary JM, Sutton C, et al. Inorganic halide double perovskites with optoelectronic properties modulated by sublattice mixing. *J Am Chem Soc*. 2020;*142*:5135–5145.
62. Chen Q, De Marco N, Yang YM, et al. Under the spotlight: the organic–inorganic hybrid halide perovskite for optoelectronic applications. *Nano Today*. 2015;*10*:355–396.
63. Kieslich G, Sun S, Cheetham AK. Solid-state principles applied to organic–inorganic perovskites: new tricks for an old dog. *Chem Sci*. 2014;*5*:4712–4715.
64. Kieslich G, Sun S, Cheetham AK. An extended tolerance factor approach for organic–inorganic perovskites. *Chem Sci*. 2015;*6*:3430–3433.
65. Shannon RD. Revised effective ionic radii and systematic studies of interatomic distances in halides and chalcogenides. *Acta Crystallogr Sect A*. 1976;*32*:751–767.
66. Travis W, Glover E, Bronstein H, Scanlon D, Palgrave R. On the application of the tolerance factor to inorganic and hybrid halide perovskites: a revised system. *Chem Sci*. 2016;*7*:4548–4556.
67. Bartel CJ, Sutton C, Goldsmith BR, et al. New tolerance factor to predict the stability of perovskite oxides and halides. *Sci Adv*. 2019;*5*:eaav0693.
68. Park NG, Grätzel M, Miyasaka T, Zhu K, Emery K. Towards stable and commercially available perovskite solar cells. *Nat Energy*. 2016;*1*:16152.

69. Li Y, Yang K. High-throughput computational design of organic-inorganic hybrid halide semiconductors beyond perovskites for optoelectronics. *Energ Environ Sci*. 2019;*12*:2233–2243.
70. Zhao XG, Yang JH, Fu Y, et al. Design of lead-free inorganic halide perovskites for solar cells via cation-transmutation. *J Am Chem Soc*. 2017;*139*:2630–2638.
71. Xiao Z, Du KZ, Meng W, Wang J, Mitzi DB, Yan Y. Intrinsic instability of $Cs_2In(I)M(III)X_6$ (M= Bi, Sb; X= halogen) double perovskites: a combined density functional theory and experimental study. *J Am Chem Soc*. 2017;*139*:6054–6057.
72. Xiao Z, Du KZ, Meng W, Mitzi DB, Yan Y. Chemical origin of the stability difference between copper(I)- and silver(I)-based halide double perovskites. *Angew Chem Int Ed*. 2017;*129*:12275–12279.
73. Hu S, Xia B, Lin YP, et al. P-type transparent quadruple perovskite halide conductors: fact or fiction? *Adv Funct Mater*. 2020;*30*:1909906.
74. Filip MR, Liu X, Miglio A, Hautier G, Giustino F. Phase diagrams and stability of lead-free halide double perovskites $Cs_2BB'X_6$: B = Sb and Bi, B' = Cu, Ag, and Au, and X = Cl, Br, and I. *J Phys Chem C*. 2018;*122*:158–170.
75. Ong SP, Wang L, Kang B, Ceder G. Li-Fe-P-O_2 phase diagram from first principles calculations. *Chem Mater*. 2008;*20*:1798–1807.
76. Huo Z, Wei SH, Yin WJ. High-throughput screening of chalcogenide single perovskites by first-principles calculations for photovoltaics. *J Phys D Appl Phys*. 2018;*51*:474003.
77. Lu S, Zhou Q, Ouyang Y, Guo Y, Li Q, Wang J. Accelerated discovery of stable lead-free hybrid organic-inorganic perovskites via machine learning. *Nat Commun*. 2018;*9*:3405.
78. Filip MR, Giustino F. Computational screening of homovalent lead substitution in organic–inorganic halide perovskites. *J Phys Chem C*. 2016;*120*:166–173.
79. McCall KM, Friedrich D, Chica DG, et al. Perovskites with a twist: strong In^{1+} off-centering in the mixed-valent $CsInX_3$ (X = Cl, Br). *Chem Mater*. 2019;*31*:9554–9566.
80. Ali R, Hou GJ, Zhu ZG, Yan QB, Zheng QR, Su G. Predicted lead-free perovskites for solar cells. *Chem Mater*. 2018;*30*:718–728.
81. Debbichi L, Lee S, Cho H, et al. Mixed valence perovskite $Cs_2Au_2I_6$: a potential material for thin-film Pb-free photovoltaic cells with ultrahigh efficiency. *Adv Mater*. 2018;*30*:1707001.
82. Polman A, Knight M, Garnett EC, Ehrler B, Sinke WC. Photovoltaic materials: present efficiencies and future challenges. *Science*. 2016;*352*:aad4424.
83. Shockley W, Queisser HJ. Detailed balance limit of efficiency of P-N junction solar cells. *J Appl Phys*. 1961;*32*:510–519.
84. Perdew JP, Burke K, Ernzerhof M. Generalized gradient approximation made simple. *Phys Rev Lett*. 1996;*77*:3865–3868.
85. Heyd J, Scuseria GE, Ernzerhof M. Hybrid functionals based on a screened coulomb potential. *J Chem Phys*. 2003;*118*:8207–8215.
86. Even J, Pedesseau L, Jancu JM, Katan C. Importance of spin–orbit coupling in hybrid organic/inorganic perovskites for photovoltaic applications. *J Phys Chem Lett*. 2013;*4*:2999–3005.
87. Giorgi G, Fujisawa JI, Segawa H, Yamashita K. Small photocarrier effective masses featuring ambipolar transport in methylammonium lead iodide perovskite: a density functional analysis. *J Phys Chem Lett*. 2013;*4*:4213–4216.
88. Xiao Z, Meng W, Wang J, Mitzi DB, Yan Y. Searching for promising new perovskite-based photovoltaic absorbers: the importance of electronic dimensionality. *Mater Horizons*. 2017;*4*:206–216.
89. Huang L, Lambrecht WR. Electronic band structure, phonons, and exciton binding energies of halide perovskites $CsSnCl_3$, $CsSnBr_3$, and $CsSnI_3$. *Phys Rev B*. 2013;*88*:165203.
90. Yin WJ, Yang JH, Kang J, Yan Y, Wei SH. Halide perovskite materials for solar cells: a theoretical review. *J Mater Chem A*. 2015;*3*:8926–8942.
91. Xiao Z, Yan Y. Progress in theoretical study of metal halide perovskite solar cell materials. *Adv Energy Mater*. 2017;*7*:1701136.
92. Saha S, Sinha TP, Mookerjee A. Electronic structure, chemical bonding, and optical properties of paraelectric $BaTiO_3$. *Phys Rev B*. 2000;*62*:8828–8834.
93. Wu L, Lu P, Li Y, Sun Y, Wong J, Yang K. First-principles characterization of two-dimensional $(CH_3(CH_2)_3NH_3)_2(CH_3NH_3)_{n-1}Ge_nI_{3n+1}$ perovskite. *J Mater Chem A*. 2018;*6*:24389–24396.
94. Li Y, Maldonado-Lopez D, Ríos Vargas V, Zhang J, Yang K. Stability diagrams, defect tolerance, and absorption coefficients of hybrid halide semiconductors: high-throughput first-principles characterization. *J Chem Phys*. 2020;*152*:084106.
95. Giorgi G, Yamashita K, Palummo M. Nature of the electronic and optical excitations of Ruddlesden–popper hybrid organic–inorganic perovskites: the role of the many-body interactions. *J Phys Chem Lett*. 2018;*9*:5891–5896.
96. Cho Y, Berkelbach TC. Optical properties of layered hybrid organic–inorganic halide perovskites: a tight-binding GW-BSE study. *J Phys Chem Lett*. 2019;*10*:6189–6196.
97. Freysoldt C, Grabowski B, Hickel T, et al. First-principles calculations for point defects in solids. *Rev Mod Phys*. 2014;*86*:253–305.
98. Kumagai Y, Oba F. Electrostatics-based finite-size corrections for first-principles point defect calculations. *Phys Rev B*. 2014;*89*:195205.
99. Lany S, Zunger A. Assessment of correction methods for the band-gap problem and for finite-size effects in supercell defect calculations: case studies for ZnO and GaAs. *Phys Rev B*. 2008;*78*:235104.
100. Broberg D, Medasani B, Zimmermann NE, et al. PyCDT: a python toolkit for modeling point defects in semiconductors and insulators. *Comput Phys Commun*. 2018;*226*:165–179.
101. He X, Xiao Z, Katase T, Ide K, Hosono H, Kamiya T. Intrinsic and extrinsic defects in layered nitride semiconductor $SrTiN_2$. *J Phys Chem C*. 2019;*123*:19307–19314.
102. Emery AA, Saal JE, Kirklin S, Hegde VI, Wolverton C. High-throughput computational screening of perovskites for thermochemical water splitting applications. *Chem Mater*. 2016;*28*:5621–5634.

103. García-Espejo G, Rodríguez-Padrón D, Luque R, Camacho L, de Miguel G. Mechanochemical synthesis of three double perovskites: $Cs_2AgBiBr_6$, $(CH_3NH_3)_2TlBiBr_6$ and $Cs_2AgSbBr_6$. *Nanoscale*. 2019;*11*:16650–16657.
104. Li YJ, Wu T, Sun L, et al. Lead-free and stable antimony–silver-halide double perovskite $(CH_3NH_3)_2AgSbI_6$. *RSC Adv*. 2017;*7*: 35175–35180.
105. Bekenstein Y, Dahl JC, Huang J, et al. The making and breaking of lead-free double perovskite nanocrystals of cesium silver–bismuth halide compositions. *Nano Lett*. 2018;*18*:3502–3508.
106. Creutz SE, Crites EN, De Siena MC, Gamelin DR. Colloidal nanocrystals of lead-free double-perovskite (elpasolite) semiconductors: synthesis and anion exchange to access new materials. *Nano Lett*. 2018;*18*:1118–1123.
107. Zhao XG, Yang D, Sun Y, et al. Cu–In halide perovskite solar absorbers. *J Am Chem Soc*. 2017;*139*:6718–6725.
108. Tran TT, Quintero MA, Arpino KE, et al. Chemically controlled crystal growth of $(CH_3NH_3)_2AgInBr_6$. *CrstEngComm*. 2018;*20*: 5929–5934.
109. Kim C, Huan TD, Krishnan S, Ramprasad R. A hybrid organic–inorganic perovskite dataset. *Sci Data*. 2017;*4*:170057.
110. Zhang T, Cai ZH, Chen S. Chemical trends in the thermodynamic stability and bandgaps of 980 halide double perovskites: a high-throughput first-principles study. *ACS Appl Mater Interfaces*. 2020;*12*:20680–20690.
111. Jain A, Voznyy O, Sargent EH. High-throughput screening of lead-free perovskite-like materials for optoelectronic applications. *J Phys Chem C*. 2017;*121*:7183–7187.
112. Peresh EY, Sidei V, Gaborets N, Zubaka O, Stercho I, Barchii I. Influence of the average atomic number of the A_2TeC_6 and $A_3B_2C_9$ (a= K, Rb, Cs, Tl(I); B= Sb, bi; C= Br, I) compounds on their melting point and band gap. *Inorg Mater*. 2014;*50*:101–106.
113. Tang G, Xiao Z, Hosono H, Kamiya T, Fang D, Hong J. Layered halide double perovskites $Cs_{3+n}M(II)_nSb_2X_{9+3n}$ (M= Sn, Ge) for photovoltaic applications. *J Phys Chem Lett*. 2018;*9*:43–48.
114. Liu Z, Zhao X, Zunger A, Zhang L. Design of mixed-cation tri-layered Pb-free halide perovskites for optoelectronic applications. *Adv Electron Mater*. 2019;*5*:1900234.
115. Harikesh P, Mulmudi HK, Ghosh B, et al. Rb as an alternative cation for templating inorganic lead-free perovskites for solution processed photovoltaics. *Chem Mater*. 2016;*28*:7496–7504.
116. Saparov B, Hong F, Sun JP, et al. Thin-film preparation and characterization of $Cs_3Sb_2I_9$: a lead-free layered perovskite semiconductor. *Chem Mater*. 2015;*27*:5622–5632.
117. Lehner AJ, Fabini DH, Evans HA, et al. Crystal and electronic structures of complex bismuth iodides $A_3Bi_2I_9$ (A = K, Rb, Cs) related to perovskite: aiding the rational design of photovoltaics. *Chem Mater*. 2015;*27*:7137–7148.
118. Boopathi KM, Karuppuswamy P, Singh A, et al. Solution-processable antimony-based light-absorbing materials beyond lead halide perovskites. *J Mater Chem A*. 2017;*5*:20843–20850.
119. Hebig JC, Kühn I, Flohre J, Kirchartz T. Optoelectronic properties of $(CH_3NH_3)_3Sb_2I_9$ thin films for photovoltaic applications. *ACS Energy Lett*. 2016;*1*:309–314.
120. Maughan AE, Ganose AM, Bordelon MM, Miller EM, Scanlon DO, Neilson JR. Defect tolerance to intolerance in the vacancy-ordered double perovskite semiconductors Cs_2SnI_6 and Cs_2TeI_6. *J Am Chem Soc*. 2016;*138*:8453–8464.
121. Saparov B, Sun JP, Meng W, et al. Thin-film deposition and characterization of a Sn-deficient perovskite derivative Cs_2SnI_6. *Chem Mater*. 2016;*28*:2315–2322.
122. Butler KT, Davies DW, Cartwright H, Isayev O, Walsh A. Machine learning for molecular and materials science. *Nature*. 2018;*559*: 547–555.
123. Tshitoyan V, Dagdelen J, Weston L, et al. Unsupervised word embeddings capture latent knowledge from materials science literature. *Nature*. 2019;*571*:95–98.
124. Schmidt J, Marques MR, Botti S, Marques MA. Recent advances and applications of machine learning in solid-state materials science. *NPJ Comput Mater*. 2019;*5*:1–36.
125. Li Z, Xu Q, Sun Q, Hou Z, Yin WJ. Thermodynamic stability landscape of halide double perovskites via high-throughput computing and machine learning. *Adv Funct Mater*. 2019;*29*:1807280.
126. Im J, Lee S, Ko TW, Kim HW, Hyon Y, Chang H. Identifying Pb-free perovskites for solar cells by machine learning. *NPJ Comput Mater*. 2019;*5*:37.
127. Saidi WA, Shadid W, Castelli IE. Machine-learning structural and electronic properties of metal halide perovskites using a hierarchical convolutional neural network. *NPJ Comput Mater*. 2020;*6*:36.
128. Xiao Z, Yan Y, Hosono H, Kamiya T. Roles of pseudo-closed s^2 orbitals for different intrinsic hole generation between Tl–Bi and In–Bi bromide double perovskites. *J Phys Chem Lett*. 2018;*9*:258–262.
129. Tang G, Xiao Z, Hong J. Designing two-dimensional properties in three-dimensional halide perovskites via orbital engineering. *J Phys Chem Lett*. 2019;*10*:6688–6694.

How to cite this article: Li Y, Yang K. High-throughput computational design of halide perovskites and beyond for optoelectronics. *WIREs Comput Mol Sci*. 2021;11:e1500. https://doi.org/10.1002/wcms.1500